International Journal of Hydrogen Energy 187 (2025) 152097

Contents lists available at ScienceDirect

International Journal of Hydrogen Energy

journal homepage: www.elsevier.com/locate/he

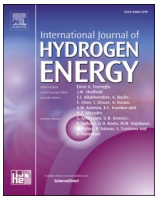

AI-driven discovery of high-performance $LiMH_x$ (M = Sc, Ti; x = 3, 4, 5) hydrides: A first-principles investigation structural, mechanical, electronic, thermophysical, optical and hydrogen storage properties

Çağatay Yamçıçıer [a,*], Sümeyra Yamçıçıer [b], Cihan Kürkçü [c]

[a] Department of Electricity and Energy, Osmaniye Korkut Ata University, Osmaniye, Türkiye
[b] Department of Physics, Osmaniye Korkut Ata University, Osmaniye, Türkiye
[c] Department of Electronics and Automation, Kırşehir Ahi Evran University, Kırşehir, Türkiye

ARTICLE INFO

Keywords:
Hydrogen storage
Complex metal hydrides
AI-driven materials discovery
Density functional theory
Lithium titanium hydrides
Lithium scandium hydrides

ABSTRACT

The pursuit of sustainable energy solutions critically depends on the development of efficient and safe hydrogen storage technologies to enable the widespread adoption of hydrogen as a clean energy carrier. While complex metal hydrides show immense promise for high-density hydrogen storage, the discovery and optimization of novel materials remain a significant challenge. This study presents the first systematic computational investigation of a novel class of hydrogen storage materials: $LiMH_x$ (M = Sc, Ti; x = 3, 4, 5) hydrides. Crucially, these materials were generated by an innovative AI-based autoregressive large language modeling (LLM) tool, representing a cutting-edge approach to materials discovery. Employing Density Functional Theory (DFT) within the CASTEP software package, we comprehensively characterize their fundamental properties. These compounds demonstrate notable thermodynamic stability, characterized by their negative enthalpies of formation (ΔH_f = −0.1912 to −0.4551 eV/atom) and positive cohesive energies. Mechanical analysis, conducted using the Born-Huang criteria, further corroborates their structural integrity. While $LiTiH_5$ exhibits the highest calculated hardness (11.51 GPa), all investigated materials display a tendency towards brittle behavior. Electronically, every compound is predicted to be metallic, a characteristic highly advantageous for facilitating rapid charge transfer and enhancing kinetic performance in hydrogen storage applications. Thermophysical assessments reveal a broad range of Debye temperatures, from a minimum of 684.64 K for $LiScH_4$ to a maximum of 911.28 K for $LiTiH_5$. Most significantly, $LiScH_4$ emerges as a particularly promising candidate for hydrogen storage, showcasing outstanding performance. It achieves an impressive gravimetric capacity of 7.21 wt%, coupled with a volumetric capacity of 123.64 gH_2/L and a favorable desorption temperature of 335.99 K. These critical metrics collectively demonstrate its ability to satisfy the rigorous targets set by the U.S. Department of Energy (DOE). Such compelling findings firmly position lithium-based hydrides as exceptionally viable materials for next-generation hydrogen storage systems, simultaneously underscoring the transformative potential of AI-assisted methodologies in expediting the discovery of advanced materials for sustainable energy solutions.

1. Introduction

The global energy landscape is currently grappling with a dual crisis: the escalating environmental degradation driven by persistent reliance on fossil fuels and the imperative to secure sustainable energy solutions for a burgeoning global population [1–3]. This predicament underscores the urgent need for a paradigm shift in energy production and consumption. Amidst various renewable alternatives, hydrogen has emerged as a particularly promising energy carrier. Its exceptional energy density, ranging from approximately 120 to 142 MJ/kg [4,5], coupled with a zero-emission combustion profile, positions it as an ideal substitute for conventional fossil fuels across diverse applications, from stationary power systems to transportation [6,7]. Furthermore, hydrogen's compatibility with renewable energy sources for its production significantly enhances its appeal for a sustainable energy future [8,9].

However, the widespread commercialization of hydrogen technologies, especially within the automotive sector, faces substantial hurdles. A primary challenge lies in the absence of efficient, safe, and cost-

* Corresponding author.
E-mail address: cagatayyamcicier@osmaniye.edu.tr (Ç. Yamçıçıer).

https://doi.org/10.1016/j.ijhydene.2025.152097
Received 11 July 2025; Received in revised form 26 September 2025; Accepted 16 October 2025
Available online 21 October 2025

effective storage methods that can meet practical operational requirements [10,11]. Current energy systems are caught in a paradox: while technological advancements continually drive increased energy demand, the continued dependence on finite fossil fuels intensifies environmental burdens through greenhouse gas emissions [1,2]. In response to these critical challenges, the U.S. Department of Energy (DOE) has established ambitious 2025 targets for hydrogen storage systems. These targets mandate stringent minimum thresholds, including a gravimetric capacity of 5.5 wt% and a volumetric density of 40 g/L, under practical operating conditions ranging from 233 to 333 K temperature and pressures below 10 MPa [12]. Achieving these benchmarks is crucial for unlocking the full potential of hydrogen as a viable and widespread energy solution.

The widespread adoption of hydrogen as a global energy carrier is critically dependent on transformative advancements in storage technology. Current solutions face the dual imperative of achieving substantial improvements in both technical performance and economic viability to meet the demands of large-scale implementation [13]. At the heart of this challenge lies a fundamental connection between a material's inherent crystalline architecture and its capacity for effective hydrogen storage. For solid-state hydrogen storage systems, the intricate processes of hydrogen sorption kinetics and thermodynamics are profoundly influenced by atomic-scale structural characteristics [14]. These include, but are not limited to, the material's unit cell geometry, crystallite morphology, and surface termination, all of which collectively dictate the available diffusion pathways for hydrogen and the specific binding energetics within the lattice [15,16]. Among the diverse array of promising material candidates, complex hydrides containing alkali or alkaline earth metals have demonstrated significant potential [17]. Their unique electronic configurations enable reversible hydrogen storage under a range of moderate temperature and pressure conditions [18], positioning them as key contenders for next-generation storage solutions [19].

Within the realm of solid-state hydrogen storage, complex metal hydrides represent a highly promising class of materials due to their ability to store hydrogen at high densities [17]. This diverse family of compounds offers significant potential for tailoring hydrogen sorption kinetics and thermodynamics through precise control over their crystalline architecture and atomic-scale structural characteristics [20]. Specifically, compounds of the general formula $LiMH_x$ (where M represents the transition metals Scandium (Sc) or Titanium (Ti), and x varies from 3 to 5) emerge as particularly intriguing candidates. The inclusion of lightweight lithium combined with the versatile bonding capabilities of transition metals like Sc and Ti allows for a wide range of tuneable hydrogen capacities and potentially favorable absorption/desorption properties [21,22]. Research into these lithium transition metal hydrides is crucial for understanding how subtle changes in stoichiometry (x) and the identity of the transition metal (M) influence structural stability, diffusion pathways, and hydrogen binding energetics, paving the way for next-generation solid-state hydrogen storage materials capable of meeting ambitious energy targets.

Recent first-principles investigations, predominantly employing density functional theory, have shed light on the potential of various lithium-containing transition metal hydrides. Siddique et al. [23], for instance, conducted a comprehensive first-principles study on $LiAH_3$ (A = Sc, Ti, & V) perovskite-type hydrides. Their work rigorously assessed the structural, electronic, mechanical, and dynamical stability, providing fundamental insights into the viability of these compounds for hydrogen storage applications. Similarly, Shah et al. [24] performed a detailed first-principles investigation of transition metal hydrides $LiXH_3$ (X = Ti, Mn, and Cu), reporting on their structural, electronic, mechanical, thermoelectric, and crucially, hydrogen storage properties. Their findings estimated a gravimetric storage capacity of 5.22 % for $LiTiH_3$, underscoring its theoretical promise as a hydrogen storage material. Moving beyond $LiMH_3$ stoichiometry, Anupam et al. [25] extended such DFT-based investigations to $LiXH_3$ (X = Pd, Ag, Cd) perovskites, examining the effects of different metal substitutions on structural, electronic, mechanical, thermoelectric, and hydrogen storage properties, further demonstrating the broad applicability of theoretical methods in this field. Furthermore, the exploration of lithium-transition metal-hydrogen systems is not limited to conventional hydrogen storage. For example, the Li–Ti–H system has been investigated under high pressure for its superconducting properties. Yang et al. [26] utilized genetic algorithms combined with DFT to explore $LiTiH_n$ (n = 1–10) within the pressure range of 50–200 GPa, identifying stable $LiTiH_4$ and $LiTiH_6$ phases and analyzing their electronic structures relevant to superconductivity. Complementary to this, Guo et al. [27] studied the structures and superconductivity of the Li–Ti–H system at even higher pressures (100–400 GPa), confirming stable $LiTiH_4$ and $LiTiH_6$ phases and predicting their superconducting transition temperatures. These high-pressure studies, while not directly focused on ambient hydrogen storage, provide invaluable data on the fundamental stability and electronic configurations of $LiTiH_x$ compounds, which can inform future design strategies. Beyond lithium-transition metal combinations, other related perovskite hydrides have also been studied. For instance, Masood et al. [28] performed a DFT study on the physical properties and hydrogen storage applications of $XScH_3$ (X = Ca, and Mg) perovskite hydrides. Their work, focusing on structural, electronic, elastic, and thermodynamic stability, provides a comparative framework for understanding the role of the alkali/alkaline earth metal in scandium-based perovskites. Similarly, Raza et al. [29] theoretically investigated $LiXH_3$ (X = Ba, Sr, Cs) perovskite hydrides, assessing their optoelectronic and thermal properties alongside hydrogen storage, further illustrating the diverse properties attainable within this class of materials.

In the literature, in addition to Li-transition metal hydrides, ABH_3-type perovskites and other complex hydride families have also been extensively studied for their hydrogen storage potential. In particular, perovskite hydrides such as $BaXH_3$ (X = Tc, Ta, and Mo) [30], $MgXH_3$ (X = Al, Sc, and Zr) [31], and KXH_3 (X = Mn, Fe) [31] provide important model systems for understanding the effects of different A and B-site cations on structural stability, hydrogen capacity, and desorption behavior. These studies have demonstrated that the compositional flexibility of the perovskite structure offers a wide scope for tuning the thermodynamic properties of the material. Similarly, complex hydrides with different stoichiometries, such as X_2CoH_5 (X = Ca, Sr) [32] and X_2TiH_6 (X = K, Ca) [33] also reveal the structural diversity and potential in this field. These previous studies establish a fundamental framework for the structure-property relationships within hydride families. This current work builds upon this foundation, specifically investigating a previously unexplored region of this compositional space with new $LiMH_x$ (M = Sc, Ti; x = 4, 5) compounds predicted by artificial intelligence. Therefore, a conceptual comparison with these well-established systems in the literature provides a critical foundation for more clearly demonstrating the novelty and relevance of the materials presented in our work.

Despite these significant theoretical advancements, the practical realization of solid-state hydrogen storage faces formidable challenges that necessitate sustained research investment and innovative solutions to overcome existing technical barriers. While numerous density functional theory studies highlight considerable progress, a substantial gap persists in translating these promising computational predictions into tangible, practical hydrogen storage applications. This study marks the inaugural systematic computational investigation of $LiMH_x$ (M = Sc, Ti, x = 3, 4, 5) hydrides, compounds uniquely identified through an AI-based autoregressive large language modeling (LLM) tool developed by Antunes et al. [34]. Herein, we comprehensively report their fundamental properties, encompassing crystal structure, mechanical behavior, electronic characteristics, thermo-physical attributes, optical response, and inherent hydrogen storage capabilities. By meticulously employing Density Functional Theory, as implemented within the CASTEP software package, this research aims to establish a crucial

theoretical framework. This foundation is designed to rigorously guide and accelerate future experimental endeavors in this nascent yet vital field.

The remainder of this paper is structured into four distinct sections for clarity and logical progression. Section 2 details the computational methodology and theoretical framework underpinning our investigations. Subsequently, Section 3 is dedicated to presenting and thoroughly analyzing the principal findings derived from our extensive simulations. Finally, Section 4 offers a concise summary of the key conclusions gleaned from this computational study, alongside a discussion of their implications for hydrogen storage applications.

2. Computational scheme

Our investigation into the ground state physical characteristics of $LiMH_x$ (M = Sc, Ti, x = 3, 4, 5) commenced with the identification of these compounds. They were initially generated by the artificial intelligence-based autoregressive large language modeling (LLM) tool developed by Antunes et al. [34]. Our computational methodology employed density functional theory (DFT), as implemented in the Cambridge Serial Total Energy Package (CASTEP) [35]. To achieve optimized crystal lattices for these materials, we utilized the Broyden-Fletcher-Goldfarb-Shanno (BFGS) geometry optimization technique [36]. Electronic exchange-correlation interactions were handled using the generalized gradient approximation (GGA) with the Perdew-Burke-Ernzerhof (PBE) functional [37]. Furthermore, ultrasoft pseudopotentials were employed to describe the electron-ion interactions for Li, Sc, Ti, and H elements [38]. The specific computational parameters were tailored for each compound to ensure accuracy: for $LiScH_3$ and $LiTiH_3$, we used an 8 × 8 × 8 Monkhorst-Pack k-point mesh [39] and a plane wave energy cutoff of 400 eV. For $LiScH_4$ and $LiScH_5$, the k-point mesh was set to 9 × 9 × 7, with an energy cutoff of 450 eV. Similarly, for $LiTiH_4$ and $LiTiH_5$, an 8 × 8 × 6 Monkhorst-Pack k-point mesh and an energy cutoff of 450 eV were applied. Geometry optimization convergence was rigorously ensured through strict thresholds: a maximum force of 0.01 eV/Å, a maximum displacement of 5×10^{-4} Å, a total energy convergence of 5×10^{-6} eV/atom, and a maximum stress of 0.02 GPa.

The elastic constants C_{ij} were determined using the "stress-strain" method within the CASTEP algorithm. These constants are fundamental for understanding the mechanical behavior and stability of materials. For materials exhibiting a cubic crystal system, the elastic constant matrix takes the following form:

$$\begin{pmatrix} C_{11} & C_{12} & C_{12} & 0 & 0 & 0 \\ C_{12} & C_{11} & C_{12} & 0 & 0 & 0 \\ C_{12} & C_{12} & C_{11} & 0 & 0 & 0 \\ 0 & 0 & 0 & C_{44} & 0 & 0 \\ 0 & 0 & 0 & 0 & C_{44} & 0 \\ 0 & 0 & 0 & 0 & 0 & C_{44} \end{pmatrix}_{Cubic} \quad \begin{pmatrix} C_{11} & C_{12} & C_{13} & 0 & 0 & 0 \\ C_{12} & C_{11} & C_{13} & 0 & 0 & 0 \\ C_{13} & C_{13} & C_{33} & 0 & 0 & 0 \\ 0 & 0 & 0 & C_{44} & 0 & 0 \\ 0 & 0 & 0 & 0 & C_{44} & 0 \\ 0 & 0 & 0 & 0 & 0 & C_{66} \end{pmatrix}_{Tetragonal}$$

From these derived elastic constants, we proceeded to estimate key mechanical properties, including the bulk modulus (B), which indicates resistance to volume change; Young's modulus (E), which measures stiffness; and shear modulus (G), representing resistance to shear deformation.

The determination of optical constants involved a meticulous analysis of photon-mediated electronic transitions occurring between occupied and unoccupied quantum states within the materials. These optical properties are fundamentally derived from the complex dielectric function $\varepsilon(\omega) = \varepsilon_1(\omega) + i\varepsilon_2(\omega)$, where its real, $\varepsilon_1(\omega)$, and imaginary, $\varepsilon_2(\omega)$, components are inherently linked through Kramers-Kronig relations. The imaginary component, which directly represents interband transitions, was computed within a momentum-space formalism using the following expression:

$$\varepsilon_2(\omega) = \frac{2e^2\pi}{\Omega\varepsilon_0}\sum_{k,v,c}\left|< \psi_k^c|\hat{u}.\vec{r}|\psi_k^v > \right|^2 \delta\left(E_k^c - E_k^v - E\right) \quad (1)$$

in this equation, Ω denotes the unit cell volume, ω is the incident photon energy, e is the electronic charge, and ψ_k^c and ψ_k^v symbolize the conduction and valence band wavefunctions at a given crystal momentum k. The delta function strictly enforces energy and momentum conservation during the optical excitation processes. Subsequently, the real component $\varepsilon_1(\omega)$ was obtained through the Kramers-Kronig transformation of $\varepsilon_2(\omega)$, thereby ensuring causality in the dielectric response. This comprehensive approach allowed for the derivation of all pertinent optical parameters, including the refractive index, $\eta(\omega)$, reflectivity, $R(\omega)$, absorption coefficient, $\alpha(\omega)$, optical conductivity, $\sigma(\omega)$, and the energy loss function $L(\omega)$ [40,41].

$$\eta(\omega) = \frac{1}{\sqrt{2}}\left[\left\{\varepsilon_1(\omega)^2 + \varepsilon_2(\omega)^2\right\}^{1/2} + \varepsilon_1(\omega)\right]^{1/2} \quad (2)$$

$$R(\omega) = \frac{(n-1)^2 + k^2}{(n+1)^2 + k^2} \quad (3)$$

$$\alpha(\omega) = \frac{4\pi k(\omega)}{\lambda} \quad (4)$$

$$\sigma(\omega) = \frac{2W_{cv}\hbar\omega}{\vec{E}_0^{\,2}} \quad (5)$$

$$L(\omega) = Im\left(-\frac{1}{\varepsilon(\omega)}\right) \quad (6)$$

The OptaDOS code was utilized to assess both the electrical density of states and the optical characteristics of the compounds [42]. For the visualization of the crystal structures, the VESTA package program was employed [43].

3. Results and analysis

3.1. Structural properties

The determined crystal structures for the $LiMH_x$ (M = Sc, Ti, x = 3, 4, 5) compounds are presented in Fig. 1(a–c). For $LiScH_3$ and $LiTiH_3$ compounds, they crystallize in a cubic structure with space group $Pm\bar{3}m$ (No. 191). The unit cell of these compounds contains one Li atom, one M (Ti or Sc) atom, and three H atoms. Within this unit cell, the Li atoms occupy the 1a (0.0, 0.0, 0.0) Wyckoff position, the M atoms are located at the 1b (0.5, 0.5, 0.5) position, and the H atoms reside at the 3c (0.0, 0.5, 0.5) positions. The $LiScH_{4/5}$ and $LiTiH_{4/5}$ compounds crystallize in a tetragonal structure with space group $P4/mmm$ (No. 123). For $LiScH_4$ and $LiTiH_4$, the unit cell comprises one Li atom, one M (Sc or Ti) atom, and four H atoms. The Li atoms are situated at the 1a (0.0, 0.0, 0.0) position, the M atoms at the 1d (0.5, 0.5, 0.5) position, and the four H atoms at the 4i (0.0, 0.5, z) positions. The fractional coordinate 'z' for the H atoms is 0.25816 for $LiScH_4$ and 0.26543 for $LiTiH_4$. In the case of $LiScH_5$ and LiTiH5, the unit cell contains one Li atom, one M (Sc or Ti) atom, and five H atoms. The Li atoms occupy the 1a (0.0, 0.0, 0.0) position, the M atoms the 1d (0.5, 0.5, 0.5) position, one H atom (H1) is at the 1c (0.5, 0.5, 0.0) position, and the remaining four H atoms (H2) are at the 4i (0.0, 0.5, z) positions. The 'z' coordinate for the H2 atoms is 0.24399 for $LiScH_5$ and 0.27305 for $LiTiH_5$.

The compounds considered in this study were generated by the artificial intelligence-based autoregressive large language modelling (LLM) model developed by Antunes et al. [34]. Table 1 presents the results of our first-principles calculations for the structural properties of these materials, including both calculated and available

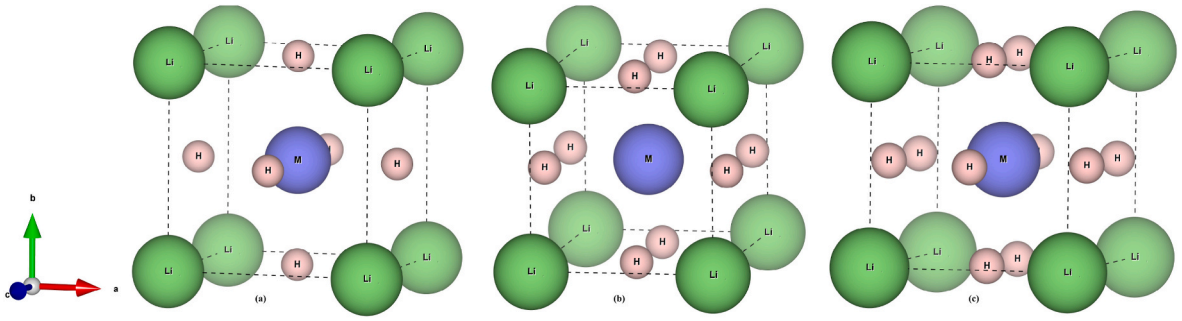

Fig. 1. Crystal structure of (a) $LiMH_3$, (b) $LiMH_4$ and (c) $LiMH_5$ (M = Sc, Ti) compounds unit cell.

Table 1
Optimized lattice constants (a, b, c in Å), unit cell volume (V in g.cm^{-3}), formation enthalpy (ΔH_f in eV/atom), and cohesive energy (E_{coh} in eV/atom) for $LiMH_x$ (M = Sc, Ti, x = 3, 4, 5) with comparative literature data.

Material	a	b	c	V	ΔH_f	E_{coh}	References
$LiScH_3$	3.3967	3.3967	3.3967	39.19	−0.3808	3.6487	This study
	3.8640	3.8640	3.8640	57.69	–	–	[44]
$LiScH_4$	3.3600	3.3600	4.7567	53.70	−0.4551	3.7302	This study
$LiScH_5$	3.2618	3.2618	4.7787	50.84	−0.2573	3.5375	This study
$LiTiH_3$	3.6096	3.6096	3.6096	47.03	−0.2066	3.9270	This study
	3.6060	3.6060	3.6060	46.91	–	–	[44]
$LiTiH_4$	3.0921	3.0921	4.7733	45.64	−0.2952	3.9472	This study
$LiTiH_5$	3.2060	3.2060	4.4284	45.52	−0.1912	3.7944	This study

theoretical/experimental lattice parameters [44]. Based on our comprehensive literature search, the $LiMH_x$ (M = Ti, Sc, x = 4, 5) structures investigated in this study are reported here for the first time.

The thermal stability of hydrides plays a crucial role in solid-state hydrogen storage, as it directly affects both the capacity and the retention time of hydrogen. To evaluate the thermal stability of $LiMH_x$ (M = Sc, Ti, x = 3, 4, 5) compounds, we calculated their standard enthalpies of formation (ΔH_f). This thermodynamic parameter provides insight into the energy released during the formation of a hydride from its elemental components and is closely related to the temperature at which hydrogen desorption occurs. Typically, hydride materials exhibit negative ΔH_f values, indicating that energy is released upon hydrogen incorporation, which in turn reflects their thermodynamic stability. A more negative ΔH_f value corresponds to a more thermodynamically stable hydride. Conversely, a positive ΔH_f suggests instability and the likelihood of decomposition under standard conditions. The enthalpy of formation was determined by calculating the difference in total energy between the products and the reactants, following the standard thermodynamic relationship:

$$\Delta H_f = \sum E^{total}_{product} - \sum E^{total}_{reactant} \tag{7}$$

This approach enables a comparative assessment of the thermal stability of the studied hydrides and aids in identifying suitable candidates for hydrogen storage applications. The ΔH_f value for $LiMH_x$ (M = Sc, Ti, x = 3, 4, 5) compounds is calculated using the following relation.

$$\Delta H_f = E_{tot}(LiM\,H_x) - \left[E_{tot}(Li) + E_{tot}(M) + \frac{x}{2}E_{tot}(H_2)\right] \tag{8}$$

The formation enthalpies for the $LiMH_x$ (M = Sc, Ti, x = 3, 4, 5) compounds are listed in Table 1. The calculated ΔH_f values for $LiScH_3$, $LiScH_4$, $LiScH_5$, $LiTiH_3$, $LiTiH_4$, and $LiTiH_5$ are −0.3808, −0.4551, −0.2573, −0.2066, −0.2952, and −0.1912 eV/atom, respectively. The negative ΔH_f values for all compounds indicate their thermodynamic stability and suggest that they can be synthesized under suitable conditions [45,46]. Among these, $LiScH_4$ shows the most negative ΔH_f value (−0.4551 eV/atom), implying it is the most thermodynamically stable phase in this series.

The cohesive energy (E_{coh}) serves as a fundamental indicator of crystalline stability, quantifying the binding strength between constituent atoms within a solid-state system. This parameter corresponds to the minimum energy required to dissociate the crystal into its isolated atomic components. Systems exhibiting positive cohesive energy values are thermodynamically favored, as this condition reflects energy release during crystal formation from free atoms. The stability assessment can be performed through the following relation:

$$E_{coh} = -\frac{1}{N}\left[E_{tot}(LiM\,H_x) - E_{tot}(Li) - E_{tot}(M) - \frac{x}{2}E_{tot}(H_2)\right] \tag{9}$$

The cohesive energy of the $LiMH_x$ (M = Sc, Ti, x = 3, 4, 5) system was determined by comparing the total energy of the compound $E_{tot}(LiM\,H_x)$, with the energies of its constituent species, namely individual Li and M atoms and molecular H_2, denoted as $E_{tot}(Li)$, $E_{tot}(M)$, and $E_{tot}(H_2)$ respectively. Here, N corresponds to the number of atoms in the unit cell.

To determine the position of our calculated formation enthalpy and cohesive energy values in the literature, our results were compared with similar hydride systems. The ΔH_f values obtained in this study (−0.1912 to −0.4551 eV/atom) and the reported values for $CsXH_3$ (X: Sc, Y) [47] compounds, such as −0.548 and −0.568 eV/atom, and with the values reported for $NaAlH_3$ (−0.43 eV/atom) and $MgAlH_3$ (−0.50 eV/atom) [48]. This consistency strongly supports the physical plausibility of our calculations and the thermodynamic stability of the $LiMH_x$ compounds studied. Similarly, the positive cohesive energy values calculated in our study (ranging from 3.53 to 3.94 eV/atom) confirm the structural stability by indicating that energy is released during the formation of crystalline isolated atoms. These findings are in complete agreement with the negative cohesive energy values reported for $CsXH_3$ (X: Sc, Y) compounds (−3.765 and −3.875 eV/atom). The difference in sign stems from differences in the definition of cohesive energy (released energy vs. binding energy) and indicates the presence of strong atomic bonds in both cases.

As presented in Table 1, the calculated cohesive energies are consistently positive, indicating an exothermic formation process where energy is released during the synthesis of the compound from its atomic and molecular constituents [49]. This energetically favorable process highlights the thermodynamic stability of the $LiMH_x$ (M = Sc, Ti, x = 3,

4, 5) phases.

3.2. Mechanical properties

Elastic properties play a fundamental role in assessing the mechanical robustness of a material under various external influences such as pressure, stress and mechanical loading. These properties provide fundamental information about the material's resistance to deformation and its ability to sustain mechanical stress without compromising its structural integrity. In the case of cubic hydrides such as $LiMH_3$ (M = Sc, Ti), the mechanical behavior is characterized by three independent elastic constants C_{11}, C_{12} and C_{44}, which describe the elastic response of the crystal along different axes. In the case of tetragonal hydrides such as $LiMH_x$ (M = Sc, Ti, x = 4, 5), the mechanical behavior is characterized by 6 independent elastic constants C_{11}, C_{12}, C_{13}, C_{33}, C_{44} and C_{66}, which describe the elastic response of the crystal along different axes. To verify the mechanical stability of these structures, it is necessary to verify compliance with the Born-Huang criteria, a set of conditions that define the thermodynamic stability limits for cubic and tetragonal systems through certain inequalities involving these elastic constants [50].

$$\{C_{11} - C_{12} > 0,\ \ C_{11} + 2C_{12} > 0, and\ C_{44} > 0\}_{cubic},$$

$$\left\{C_{11} > |C_{12}|,\ 2C_{13}^2 < C_{33}(C_{11} + C_{12}),\ C_{44} > 0, C_{66} > 0\right\}_{tetragonal}$$

As can be seen in Table 2, $LiMH_x$ (M = Sc, Ti, x = 3, 4, 5) compounds have a mechanical stability that meets the criteria given above.

The elastic constants C_{11} and C_{33} reflect the material's capacity to resist uniaxial compression along the [100] and [001] crystallographic directions, respectively. These constants serve as key indicators of the lattice's ability to withstand linear stress while maintaining structural integrity, thereby offering a critical assessment of mechanical stiffness along these specific orientations. Notably, the higher C_{11} values observed in $LiMH_x$ (M = Sc, Ti, x = 4, 5) compounds compared to C_{33} suggest a greater resistance to compression along the [100] direction relative to other crystallographic axes. Additionally, the elastic constant C_{44} measures the material's resistance to shear deformation under tangential stress applied along the [010] direction within the (001) plane. A lower C_{44} value relative to C_{11} and C_{33} indicates a reduced ability to resist shear, implying that the material is more prone to shear-induced structural alterations than to compressive deformation along the same orientations. As detailed in Table 2, the $LiMH_x$ (M = Sc, Ti, x = 4, 5) compounds exhibit characteristics consistent with heightened sensitivity to shear deformations, underscoring their distinct mechanical behavior under varying stress conditions.

The shear constant $\left(C' = \frac{C_{11}-C_{12}}{2}\right)$ serves as a pivotal metric for evaluating the dynamic stability of crystalline materials. This parameter quantifies the material's resistance to shear deformation when subjected to shear stress along the [110] direction within the (100) plane. Furthermore, the shear constant provides a reliable indicator of the crystal's stable or unstable state, where a negative value signifies dynamic instability, and a positive value denotes dynamic stability. The computed shear constants for the $LiMH_x$ (M = Sc, Ti, x = 3, 4, 5) compounds are presented in Table 2. Analysis reveals that the shear constants for all investigated compounds are positive, confirming their dynamic stability and suggesting robust structural integrity under shear stress conditions.

The Kleinman parameter $\left(\zeta = \frac{C_{11}+8C_{12}}{7C_{11}+2C_{12}}\right)$ serves as a valuable metric for characterizing the internal strain response of a material, specifically quantifying the relative displacement between cation and anion sublattices under volume-conserving distortions, particularly relevant when atomic positions are not fixed by crystal symmetry. This parameter is a crucial indicator of a material's resilience against both stretching and bending deformations [51]. Defined within the range of 0–1 ($0 \le \zeta \le 1$), the parameter's bounds provide insights into the dominant deformation mechanisms. A value of $\zeta = 0$ indicates that bond bending contributions to resisting external stress are negligible, while $\zeta = 1$ implies that resistance is primarily governed by bond bending, with bond stretching/compression having a minimal effect. For the $LiMH_x$ (M = Sc, Ti, x = 3, 4, 5) compounds investigated, the calculated ζ values span from 0.26 to 0.53, specifically determined as 0.26 ($LiScH_3$), 0.40 ($LiScH_4$), 0.34 ($LiScH_5$), 0.34 ($LiTiH_3$), 0.53 ($LiTiH_4$), and 0.31 ($LiTiH_5$). These intermediate ζ values, falling between the 0 and 1 extremes, suggest that the mechanical strength and resistance to deformation in these compounds are influenced by a significant interplay of both bond bending and bond stretching/compression contributions.

The elastic behavior of solid materials is fundamentally characterized by two primary parameters: the bulk modulus (B) and the shear modulus (G). These moduli are crucial for understanding a material's mechanical response under different stress conditions. Specifically, the bulk modulus quantifies a material's resistance to volume change under hydrostatic pressure, effectively indicating its compressibility and resistance to fracture under uniform compression. In parallel, the shear modulus measures a material's stiffness against shape deformation under shear stress, reflecting its resistance to plastic flow in polycrystalline forms. The values for the bulk and shear moduli in this study were derived from the calculated elastic constants using the well-established Voigt-Reuss-Hill (VRH) approximations, as detailed in Refs. [52–54].

$$B_H = \frac{B_V + B_R}{2} \quad and \quad G_H = \frac{G_V + G_R}{2} \tag{10}$$

In this analysis, the bulk (B) and shear (G) moduli were evaluated using both the Voigt and Reuss approximations, denoted as B_V, G_V and B_R, G_R, respectively. These approximations provide upper and lower bounds for the elastic constants of polycrystalline materials. The corresponding Voigt–Reuss–Hill averages were subsequently used to derive the macroscopic elastic properties. Based on the averaged B and G values, the Young's modulus (E) and Poisson's ratio (ν) were calculated using the standard isotropic elasticity relations. This approach enables a comprehensive assessment of the material's stiffness and deformation

Table 2
Calculated independent elastic constants C_{ij} (GPa), shear constant C′, and Kleinman parameter (ζ) for $LiMH_x$ (M = Sc, Ti, x = 3, 4, 5) crystals.

Parameters	$LiScH_3$	$LiScH_4$	$LiScH_5$	$LiTiH_3$	$LiTiH_4$	$LiTiH_5$	References
C_{11}	179.30 193.74	128.84	146.99	140.89 172.59	138.06	177.94	This study [44]
C_{33}		97.53	73.61		110.95	124.76	This study
C_{44}	44.66 46.01	17.02	28.71	29.07 53.69	29.52	68.66	This study [44]
C_{66}		47.99	60.24		52.42	35.94	This study
C_{12}	19.18 17.24	31.63	23.06	26.04 73.58	41.03	24.22	This study [44]
C_{13}		13.00	34.23		25.41	30.26	This study
C'	80.06 88.25	48.60	61.97	57.42 49.51	48.51	76.86	This study [44]
ζ	0.26	0.40	0.34	0.34	0.53	0.31	This study

characteristics under mechanical loading.

$$E = \frac{9GB}{(3B+G)} \quad and \quad \nu = \frac{(3B-2G)}{2(3B+G)} \tag{11}$$

Young's modulus (E) is a key mechanical parameter that quantifies a material's resistance to elastic deformation under uniaxial tensile or compressive stress. It is also closely associated with the intrinsic hardness of a material. Analysis of the computed E values for the investigated $LiMH_x$ (M = Sc, Ti, x = 3, 4, 5) compounds indicates that, within the Ti-based series, $LiTiH_5$ exhibits greater stiffness and inferred hardness compared to $LiTiH_4$ and $LiTiH_3$. Similarly, in the Sc-based series, $LiScH_3$ demonstrates a higher Young's modulus than both $LiScH_4$ and $LiScH_5$. The numerical values supporting these observations are presented in Table 3. Additionally, a comparison of the bulk modulus (B) and shear modulus (G) reveals that B consistently exceeds G across all compositions. This trend implies that the mechanical stability of $LiMH_x$ (M = Sc, Ti, x = 3, 4, 5) compounds is more significantly governed by their resistance to shear deformation. Consequently, these materials are more susceptible to mechanical failure through shape distortion rather than volumetric compression under applied stress.

In material science, Pugh's ratio, expressed as the quotient of the bulk modulus (B) and the shear modulus (G), is widely recognized as a fundamental metric for assessing whether a material exhibits ductile or brittle behavior [55]. The bulk modulus reflects a material's ability to withstand uniform compression, whereas the shear modulus indicates its resistance to shear-induced deformation. According to the established Pugh criterion, a threshold value of 1.75 delineates the boundary between ductility and brittleness: materials with a B/G ratio exceeding 1.75 are deemed ductile, while those with a ratio below this value are classified as brittle. Analysis of the B/G ratios for $LiMH_x$ (M = Sc, Ti, x = 3, 4, 5) compounds, as reported in Table 3, reveals that all values fall below this critical threshold of 1.75. Consequently, these compounds demonstrate brittle properties. This characteristic implies that $LiMH_x$ (M = Sc, Ti, x = 3, 4, 5) materials are susceptible to fracturing with little to no plastic deformation, a factor that warrants careful consideration when evaluating their suitability for structural or functional purposes.

Poisson's ratio (υ) is an essential mechanical property that characterizes how a material deforms laterally in response to an applied axial strain under uniaxial loading conditions. For isotropic materials, its theoretical limits are well-established, ranging from −1.0 to 0.5 [56], encapsulating the spectrum of elastic deformation behaviors. A Poisson's ratio of 0.5 signifies isochoric deformation, where the material's volume remains constant during elastic straining [57]. Beyond its role in deformation, this ratio offers valuable insights into a material's mechanical behavior, particularly its failure tendencies. A critical value of $\upsilon = 0.26$ serves as a dividing line: materials with $\upsilon > 0.26$ typically display ductile properties, capable of undergoing significant plastic deformation, whereas those with $\upsilon < 0.26$ are predisposed to brittle fracture, fracturing with minimal plasticity. Additionally, Poisson's ratio sheds light on a material's ability to resist shear deformation, reinforcing its importance in evaluating mechanical performance. Data from Table 3 reveal that the Poisson's ratio of $LiMH_x$ (M = Sc, Ti, x = 3, 4, 5) compounds falls below the 0.26 threshold, indicating their brittle character. This suggests that these compounds are likely to fracture abruptly under stress, without substantial plastic deformation. Furthermore, Poisson's ratio provides a window into the nature of interatomic interactions within crystalline structures. When υ lies between 0.25 and 0.50, central force interactions those acting along the line connecting atomic pairs predominantly govern the bonding [58,59]. Conversely, values outside this range point to the influence of non-central forces, which involve more complex, directionally dependent interactions. Since the Poisson's ratio of $LiMH_x$ (M = Sc, Ti, x = 3, 4, 5) compounds lies outside the 0.25 to 0.50 range, it can be deduced that non-central forces significantly shape their interatomic bonding, potentially impacting their structural stability and mechanical properties. This interplay of brittleness and bonding characteristics underscores the utility of Poisson's ratio in understanding the behavior of such materials.

Machinability represents a critical attribute of materials, defining how readily they can be shaped or finished using cutting tools. This property is essential in the field of engineering, particularly within manufacturing and industrial production, where it significantly impacts decisions regarding tool selection, process optimization, and production efficiency. The ease or challenge of machining a material arises from a combination of factors, including the inherent qualities of the workpiece, the design and composition of the cutting tool, and the operational settings of the machining process. Specifically, variables such as tool material composition, tool shape, cutting velocity, applied force, feed rate, and cutting depth are closely tied to the material's machinability. Beyond its influence on machining operations, this property also provides valuable insights into a material's plasticity [60,61] and its ability to exhibit dry lubrication characteristics, shedding light on how it responds to the mechanical stresses of machining. To quantify machinability, the machinability index (μ^M) is employed, calculated through an established equation detailed in Ref. [62].

$$\mu^M = \frac{B}{C_{44}} \tag{12}$$

A higher μ^M value signifies superior machinability, indicating that the material can be processed with greater ease and precision. In this study, the machinability of various hydride phases was assessed, revealing significant variations influenced by their chemical compositions. Among the scandium-based hydrides, $LiScH_4$ achieved the highest machinability index of 3.02, outperforming $LiScH_5$ ($\mu^M = 2.05$) and $LiScH_3$ ($\mu^M = 1.62$). In the titanium-based group, $LiTiH_3$ recorded the highest index at 2.21, followed closely by $LiTiH_4$ ($\mu^M = 2.13$), with $LiTiH_5$ trailing significantly at 1.04. Across all compounds examined, $LiScH_4$ emerged as the standout performer, demonstrating exceptional machinability. This is largely due to its ideal interplay of strong interatomic bonds and favorable shear softening behavior, which together facilitate superior processing outcomes. Conversely, $LiTiH_5$ exhibited the lowest machinability index, suggesting it is the least processable among the studied materials. These findings highlight the pivotal role of chemical composition in determining a material's machinability. The observed differences in μ^M values across the hydride phases illustrate how atomic-level variations can profoundly affect material removal efficiency. Such insights are essential for advancing the development of

Table 3
Voigt-Reuss-Hill averaged bulk modulus (B), shear modulus (G), Young's modulus (E), Pugh's ratio (B/G), Poisson's ratio (ν), and machinability index (μ^M) for $LiMH_x$ (M = Sc, Ti, x = 3, 4, 5) compounds.

Compound	B_R	B_V	B_H	G_R	G_V	G_H	E	B/G	υ	μ^M	References
$LiScH_3$	72.56	72.56	72.56	54.26	58.82	56.54	134.64	1.28	0.19	1.62	This study [44]
			65.07			43.73	142.34	1.48	0.19		
$LiScH_4$	50.45	52.28	51.36	27.87	36.24	32.06	79.61	1.60	0.24	3.02	This study
$LiScH_5$	56.41	61.18	58.80	36.11	41.94	39.02	95.86	1.51	0.23	2.05	This study
$LiTiH_3$	64.32	64.32	64.32	36.22	40.41	38.31	95.91	1.68	0.25	2.21	This study [44]
			88.51			45.98		1.92	0.29		
$LiTiH_4$	62.06	63.42	62.74	39.08	41.97	40.53	100.04	1.55	0.23	2.13	This study
$LiTiH_5$	70.74	72.24	71.49	56.50	61.05	58.78	138.40	1.22	0.18	1.04	This study

high-performance machinable alloys, particularly in precision engineering and manufacturing contexts where optimal material processability is a priority.

3.3. Hardness

Hardness is a key property that measures a material's ability to endure permanent deformation under localized mechanical forces, playing an essential role in evaluating structural integrity within engineering disciplines. This characteristic provides valuable insights into how materials perform when exposed to intense loading conditions, making it a critical factor for predicting reliability in harsh operational environments. Among the array of mechanical properties, the elastic constant C_{44} and the shear modulus stand out as robust indicators of intrinsic hardness, demonstrating a strong connection to a material's capacity to resist plastic deformation [63]. The analysis of hardness in this study relies on a range of theoretical computational techniques, each distinguished by its specific strengths in delivering accurate predictions. Hardness values were determined using well-established models proposed by Teter et al. [64], Tian et al. [65], Miao et al. [66], Mazhnik et al. [67], and Chen et al. [68]. These frameworks were chosen for their proven effectiveness in assessing hardness across diverse material types. The detailed equations utilized for these computations are presented follow.

$$(H_V)_{miao} = \frac{(1-2\nu)E}{6(1+\nu)} \tag{13}$$

$$(H_V)_{Chen} = 2\left[\left(\frac{G}{B}\right)^2 G\right]^{0.585} - 3 \tag{14}$$

$$(H_V)_{Tian} = 0.92\left(G/B\right)^{1.137} G^{0.708} \tag{15}$$

$$(H_V)_{Teter} = 0.151G \tag{16}$$

$$(H_V)_{Mazhnik} = \gamma_0 \frac{1 - 8.5\sigma + 19.5\sigma^2}{1 - 7.5\sigma + 12.2\sigma^2 + 19.6\sigma^3} E \tag{17}$$

Also γ_0 is a dimensionless constant with a value of 0.096.

The $(H_V)_{miao}$, $(H_V)_{Chen}$, $(H_V)_{Tian}$, $(H_V)_{Teter}$, and $(H_V)_{Mazhnik}$ values obtained for the $LiMH_x$ (M = Sc, Ti, x = 3, 4, 5) compounds are presented in Table 4.

The calculated hardness values for the $LiMH_x$ (M = Sc, Ti, x = 3, 4, 5) hydrides reveal clear compositional and methodological trends (Table 4). In the Sc-based series, $LiScH_3$ exhibits the greatest resistance to indentation, with an average hardness of 10.54 GPa, whereas $LiScH_4$ (5.21 GPa) and $LiScH_5$ (6.54 GPa) are substantially softer. A similar pattern emerges in the Ti-based compounds: $LiTiH_5$ demonstrates the highest stiffness against plastic deformation (11.51 GPa), followed by $LiTiH_4$ (6.61 GPa) and $LiTiH_3$ (5.91 GPa). Across all compositions, the individual hardness models (Chen, Tian, Teter, Miao, and Mazhnik) display consistent relative ordering, although absolute values differ by up to ~50 %, reflecting varying sensitivities to bond character and crystal topology. The pronounced hardness of the M = Sc and M = Ti compounds with "3" stoichiometry suggests a more rigid lattice framework likely due to optimal cation–anion bonding balance whereas higher hydrogen content (x = 4, 5) weakens the network through increased bond flexibility. These findings underscore the utility of multiple semi-empirical models in capturing the mechanical resilience of hydrogen-rich frameworks and point to $LiScH_3$ and $LiTiH_5$ as the most mechanically robust candidates for hydrogen storage applications.

3.4. Elastic anisotropy

Elastic anisotropy is a fundamental property of crystalline solids, characterized by mechanical responses that vary with the direction of applied stress. This attribute plays a pivotal role in shaping key material processes, including the motion of dislocations, the progression of cracks, and the mechanisms of fracture, particularly within systems exhibiting structural asymmetry. The origin of this directional dependence lies in the crystallographic framework, where lattice asymmetry dictates the variation in elastic behavior. Such understanding is indispensable for the development of cutting-edge materials and the design of structures capable of withstanding imperfections. The compound $LiMH_x$ (M = Sc, Ti, x = 3, 4, 5) emerges as a noteworthy subject for examining how atomic bonding influences anisotropic characteristics. Detailed scrutiny of its elastic anisotropy is essential to unravel how it performs under multifaceted stress conditions. Specifically, crystals featuring covalent bonds, with their localized electron distributions, tend to display marked anisotropy. In contrast, those with metallic bonds, characterized by freely shared electrons, exhibit a tendency toward isotropic behavior [69]. This interplay between bonding type and mechanical properties underscores the importance of elastic anisotropy in predicting and optimizing material performance for advanced engineering applications.

The degree of elastic anisotropy in solid materials, which reflects the directional dependence of their mechanical properties, is quantitatively assessed using dimensionless metrics such as the Zener anisotropy parameter ($A = \frac{2C_{44}}{C_{11}-C_{12}}$). Calculated following the formalism outlined by Yang et al. [70], the Zener parameter serves as a key indicator: a value of A = 1 signifies isotropic elastic behavior, where mechanical response is uniform in all directions. Conversely, deviations from unity (A = 1) denote anisotropic elasticity, with larger deviations correlating to a more pronounced direction-dependent mechanical response. For the $LiMH_x$ (M = Sc, Ti, x = 3, 4, 5) compounds, our calculations yielded Zener anisotropy parameter values indicating varying degrees of anisotropy: $LiScH_3$ (A = 0.5579), $LiScH_4$ (A = 0.3502), $LiScH_5$ (A = 0.4633), $LiTiH_3$ (A = 0.5062), $LiTiH_4$ (A = 0.6084), and $LiTiH_5$ (A = 0.8934). These values, all differing from 1, confirm the presence of elastic anisotropy in these materials. Further insight into the directional asymmetry of bonding and resistance to deformation can be gained from shear anisotropic factors. These factors specifically quantify the differential resistance to shear deformation across distinct crystallographic planes. For cubic and tetragonal crystal systems, a complete characterization of shear anisotropy necessitates the evaluation of three independent parameters derived from directional elastic constants [71,72].

Shear anisotropy factor between ⟨011⟩ and ⟨010⟩ directions for shear plane {100},

Table 4
Comparative theoretical hardness predictions (GPa) using the Chen, Tian, Teter, Miao, and Mazhnik models with averaged values for $LiMH_x$ (M = Sc, Ti, x = 3, 4, 5) compounds.

Compound	$(H_V)_{Chen}$	$(H_V)_{Tian}$	$(H_V)_{Teter}$	$(H_V)_{Miao}$	$(H_V)_{Mazhnik}$	$(H_V)_{avg}$
$LiScH_3$	12.83	12.06	8.54	11.66	7.63	10.54
$LiScH_4$	5.76	6.27	4.84	5.52	3.66	5.21
$LiScH_5$	7.56	7.73	5.89	7.07	4.45	6.54
$LiTiH_3$	6.21	6.75	5.79	6.35	4.47	5.91
$LiTiH_4$	7.46	7.70	6.12	7.18	4.61	6.61
$LiTiH_5$	14.24	13.17	8.88	12.64	8.63	11.51

$$A_1 = \frac{4C_{44}}{C_{11} + C_{33} - 2C_{13}} \tag{18}$$

Shear anisotropy factor between ⟨101⟩ and ⟨001⟩ directions for shear plane {010},

$$A_2 = \frac{2C_{55}}{C_{22} + C_{33} - 2C_{23}} \tag{19}$$

Shear anisotropy factor between ⟨110⟩ and ⟨010⟩ directions for shear plane {001},

$$A_3 = \frac{4C_{66}}{C_{11} + C_{22} - C_{12}} \tag{20}$$

The shear anisotropy factors A_1, A_2, and A_3 calculated for the $LiMH_x$ (M = Sc, Ti, x = 3, 4, 5) compounds provide valuable insights into the directional dependence of their mechanical behavior. As presented in the table, A_1 and A_2 exhibit identical values across all compositions, reflecting similar anisotropic shear responses between the specified crystallographic directions on the {100} and {010} shear planes. Notably, $LiTiH_5$ displays the highest values for these parameters (1.1341), indicating a pronounced anisotropy and suggesting that shear deformation along these directions will be highly direction dependent. In contrast, the other compounds show considerably lower A_1 and A_2 values, with $LiScH_4$ presenting the smallest anisotropy (0.3398), implying a relatively more isotropic shear response in those planes. The A_3 values vary more distinctly among the compounds, highlighting differences in shear anisotropy on the {001} shear plane. $LiScH_4$ and $LiScH_5$ exhibit values close to unity (0.9874 and 0.9721, respectively), indicative of nearly isotropic shear resistance along the compared directions. Conversely, $LiTiH_4$ shows a higher A_3 value (1.0804), suggesting increased anisotropy, while $LiTiH_5$ and $LiTiH_3$ present lower values (0.4677 and 0.5062), indicating more isotropic or less pronounced anisotropic behavior in this shear system. Overall, these anisotropy factors reveal that shear deformation in $LiMH_x$ (M = Sc, Ti, x = 3, 4, 5) hydrides is directionally dependent, with variations influenced both by the type of metal cation and hydrogen content. This anisotropy has important implications for understanding slip behavior, plasticity, and mechanical reliability in these hydrogen storage materials.

In the study of material properties, the anisotropic nature of solids emerges as a pivotal factor influencing their mechanical behavior. To measure this directional dependence, a suite of indices has been established, including the universal anisotropy index (denoted as A^U and d_E), the equivalent Zener anisotropy measure (A^{eq}), the shear anisotropy (A_G), and the compressibility anisotropy (A_B). These indices are calculated using well-established mathematical formulations that apply universally to solids, regardless of their crystal symmetry, highlighting their broad utility in material science investigations. Together, these parameters deliver a detailed evaluation of anisotropy, shedding light on the mechanical properties of materials and revealing how these characteristics shift with direction. The computations rely on standard equations, as meticulously outlined in the referenced studies [73–76]. Such insights into anisotropic behavior are vital for advancing the design and optimization of materials in engineering contexts, where directional properties play a critical role in determining performance.

$$A^U = \frac{B_V}{B_R} + 5\frac{G_V}{G_R} - 6 \geq 0, d_E = \sqrt{A^U + 6} \tag{21}$$

$$A^{eq} = \left(1 + \frac{5}{12}A^U\right) + \sqrt{\left(1 + \frac{5}{12}A^U\right)^2 - 1} \tag{22}$$

$$A_B = \frac{B_V - B_R}{B_V + B_R}, A_G = \frac{G_V - G_R}{G_V + G_R} \tag{23}$$

In material science, the directional dependence of physical properties termed anisotropy plays a pivotal role in determining a material's functionality. The Universal Anisotropy Index (A^U) stands out as a versatile tool for evaluating this property across diverse crystallographic symmetries. By incorporating both shear and bulk modulus contributions, A^U provides a comprehensive perspective on anisotropic behavior, distinguishing it from conventional metrics. According to Equation (21), the ratio of Voigt to Reuss shear moduli (G_V/G_R) predominantly influences A^U, overshadowing the impact of the bulk moduli ratio (B_V/B_R). Isotropic materials exhibit an A^U value of zero, whereas non-zero values positive or negative reflect the presence and degree of elastic anisotropy. In this study, A^U calculations for Sc-based hydrides yielded values of 0.4200, 1.5387, and 0.8920, while those for Ti-based hydrides were 0.5780, 0.3912, and 0.4231. These findings confirm the pronounced anisotropic character of both material groups.

The computed A^{eq} values for $LiMH_x$ (M = Sc, Ti, x = 3, 4, 5) compounds are presented in Table 5. The compressibility anisotropy index (A_B) and shear anisotropy index (A_G) each range between 0 and 1, where a value of 1 reflects the maximum degree of anisotropy and a value of 0 signifies complete isotropy. Examination of the data in Table 5 indicates that $LiScH_3$ and $LiTiH_3$ exhibit isotropic properties in terms of compressibility. Conversely, the other compounds under study display anisotropic characteristics in both shear and compressibility. Across all $LiMH_x$ (M = Sc, Ti, x = 3, 4, 5) compounds analyzed, the A_G values consistently surpass their corresponding A_B values, suggesting that shear anisotropy exerts a more dominant influence than compressibility anisotropy in these material systems (see Table 6).

The following defines the universal log-Euclidean anisotropy index [70]:

$$A^L = \sqrt{\left[ln\left(\frac{B_V}{B_R}\right)\right]^2 + 5\left[ln\left(\frac{C_{44}^V}{C_{44}^R}\right)\right]^2} \tag{24}$$

In the study of elastic properties, the constants $C_{44}^V = \frac{3}{5}\frac{(C_{11}-C_{12}-2C_{44})}{3(C_{11}-C_{12})+4C_{44}}$ and $C_{44}^R = \frac{5}{3}\frac{C_{44}(C_{11}-C_{12})}{3(C_{11}-C_{12})+4C_{44}}$ are defined as the Voigt and Reuss approximations, respectively, of the elastic constant C_{44}. A central element of this investigation is the A^L anisotropy parameter, which is universally applicable across all crystal symmetries, much like the universal anisotropy index (A^U). With proper scaling, A^L accurately reflects perfect isotropy and maintains its effectiveness across diverse crystallographic point groups. For materials exhibiting significant anisotropy, A^L proves to be a more suitable metric than A^U due to its lower sparsity, offering a clearer depiction of anisotropic tendencies.

The universal anisotropy index (A^U), while useful, falls short in fully representing the absolute extent of anisotropy, as noted in prior research [69]. In contrast, the A^L parameter, when evaluated alongside the mean hardness values from the Voigt (C^V) and Reuss (C^R) methods, provides a more dependable measure of anisotropy. The range of A^L values extends from 0 to a maximum of 10.26, with over 90 % of solids having values below 1. An A^L value of zero denotes a perfectly isotropic material. For Sc-based hydrides, the calculated AL values are 0.5030, 1.3981, and 0.8312, respectively. For Li-based hydrides, the values are 0.6658, 0.3735, and 0.0292, respectively. Among the Sc-based hydrides, $LiScH_4$ with a value of 1.3981 exceeding 1 indicates a significant departure

Table 5
Elastic anisotropy parameters of $LiMH_x$ (M = Sc, Ti, x = 3, 4, 5) compounds.

Parameters	$LiScH_3$	$LiScH_4$	$LiScH_5$	$LiTiH_3$	$LiTiH_4$	$LiTiH_5$
A	0.5579	0.3502	0.4633	0.5062	0.6084	0.8934
A_1	0.5579	0.3398	0.7548	0.5062	0.5957	1.1341
A_2	0.5579	0.3398	0.7548	0.5062	0.5957	1.1341
A_3	0.5579	0.9874	0.9721	0.5062	1.0804	0.4677
A_B	0.0000	0.0178	0.0406	0.0000	0.0108	0.0104
A_G	0.0400	0.1306	0.0747	0.0546	0.0356	0.0387
A^U	0.4200	1.5387	0.8920	0.5780	0.3912	0.4231
d_E	2.5340	2.7457	2.6253	2.5648	2.5281	2.5344
A^{eq}	1.7920	2.9424	2.3106	1.9755	1.7568	1.7958
A^L	0.5030	1.3981	0.8312	0.6658	0.3735	0.0292

Table 6
Bulk modulus (B_{relax} in GPa), bulk modulus along the a-, b-, and c-axes (B_a, B_b, and B_c in GPa), and α and β of $LiMH_x$ (M = Sc, Ti, x = 3, 4, 5) compounds.

Compound	B_{relax}	B_a	B_b	B_c	α	β	A_{B_a}	A_{B_c}
$LiScH_3$	72.56	217.67	217.67	217.67	1.00	1.00	1.00	1.00
$LiScH_4$	50.45	181.15	181.15	113.87	1.00	1.59	1.00	0.63
$LiScH_5$	56.41	258.37	258.37	100.14	1.00	2.58	1.00	0.39
$LiTiH_3$	64.32	192.96	192.96	192.96	1.00	1.00	1.00	1.00
$LiTiH_4$	62.06	217.20	217.20	144.84	1.00	1.50	1.00	0.67
$LiTiH_5$	70.74	247.51	247.51	165.14	1.00	1.50	1.00	0.67

from isotropy, while the other two values below 1 indicate moderate anisotropy. Conversely, Li-based hydrides with A^L values of 0.6658, 0.3735 and 0.0292 all below 1 show a trend towards lower anisotropy. In particular, the value of 0.0292 ($LiTiH_5$) approaches zero, indicating near isotropic behavior in one of the samples. These results emphasize the effectiveness of the A^L parameter in distinguishing nuanced differences in anisotropy, especially in cases where the A^U may lack sensitivity. The integration of the Voigt and Reuss approaches further enriches this analysis by accounting for both shear and bulk contributions to material behavior. Research indicates that materials with elevated A^L values typically possess a layered structure, whilst those with diminished A^L values are generally non-layered [75,77]. Strong layered and non-layered structural materials can be forecast from the higher and lower values of A^L, respectively. The estimated value for $LiMH_x$ (M = Sc, Ti, x = 3, 4, 5) compounds suggests that this compound does not show notable layered kind of structural structure since the value of A^L is relatively low.

The bulk modulus and its anisotropies along the a, b, and c axes can be obtained using the following formulae [78].

$$B_a = a\frac{dP}{da} = \frac{\Lambda}{1+\alpha+\beta}, \quad B_b = b\frac{dP}{db} = \frac{B_a}{\alpha}, \quad B_c = c\frac{dP}{dc} = \frac{B_a}{\beta} \tag{26}$$

$$B_{relax} = \frac{\Lambda}{(1+\alpha+\beta)^2} \tag{27}$$

where $\Lambda = C_{11} + 2C_{12}\alpha + C_{22}\alpha^2 + 2C_{13}\beta + C_{33}\beta^2 + 2C_{23}\alpha\beta$ and

$$\alpha = \frac{\{(C_{11}-C_{12})(C_{33}-C_{13})\} - \{(C_{23}-C_{13})(C_{11}-C_{13})}{\{(C_{33}-C_{13})(C_{22}-C_{12})\} - \{(C_{13}-C_{23})(C_{12}-C_{23})\}}$$

$$\beta = \frac{\{(C_{22}-C_{12})(C_{11}-C_{13})\} - \{(C_{11}-C_{12})(C_{23}-C_{12})\}}{\{(C_{22}-C_{12})(C_{33}-C_{13})\} - \{(C_{12}-C_{23})(C_{13}-C_{23})\}}$$

B_{relax} represents the average compressibility of the system under hydrostatic pressure. A higher B_{relax} value means lower compressibility and higher structural stiffness. Among the Sc-based compounds, the highest B_{relax} value of 72.56 GPa indicates that $LiScH_3$ compound is the least compressible structure, while $LiScH_4$ compound with the lowest B_{relax} value is more easily compressible. Among the Ti based compounds, $LiTiH_5$ compound with 70.74 GPa is the least compressible structure and $LiTiH_4$ compound with the lowest B_{relax} value shows that it is more easily compressible. The directional volume moduli B_a, B_b and B_c refer to the mechanical stiffness in the a, b and c directions along the crystal structure. For $LiScH_4$, $LiScH_5$, $LiTiH_4$ and $LiTiH_5$ compounds, $B_a = B_b$ is greater than B_c, indicating that these compounds are more compressible along the c direction.

The bulk modulus anisotropies along the a and c axes with respect to the b axis are expressed as:

$$A_{B_a} = \frac{B_a}{B_b}, \quad A_{B_c} = \frac{B_c}{B_b} \tag{28}$$

An A_{B_a} value of 1 for all compounds indicates symmetric bond strength in the a and b directions. A_{B_c} indicates the mechanical behavior along the c-axis compared to the a-axis. Low values such as $LiScH_4$ (0.63), $LiScH_5$ (0.39) and $LiTiH_{4/5}$ (0.67) reveal weakness along the c-axis. The values of 1.00 in $LiScH_3$ and $LiTiH_3$ support that they have a 3D bonding pattern and are isotropic.

To rigorously assess the anisotropic behavior of the investigated compounds, we utilized three-dimensional (3D) surface representations of their elastic properties, generated with the VELAS software package [79]. This tool enables accurate visualization of directional dependencies in mechanical responses. A detailed summary of the elastic properties including Young's modulus, bulk modulus, shear modulus, and stiffness, along with their respective extrema is provided in Table 7, offering a robust basis for comparing mechanical characteristics across various compositions. The 3D representations for Sc-based and Ti-based hydrides are illustrated in Figs. 2(a–c) and 3 (a-c), respectively. In these plots, a perfectly spherical shape signifies complete isotropy across all dimensions, whereas deviations from sphericity indicate anisotropic tendencies in specific directions. The bulk moduli of $LiScH_3$ and $LiTiH_3$ display spherical symmetry, confirming their isotropic nature. However, their Young's modulus, shear modulus, bulk modulus, and hardness exhibit deviations from sphericity, revealing marked anisotropy across all planes. Similarly, for $LiScH_{4/5}$ and $LiTiH_{4/5}$, consistent deviations in all evaluated elastic properties highlight pronounced anisotropy in every direction examined.

The mechanical properties detailed in these sections provide critical information regarding the practical applicability of $LiMH_x$ compounds as potential hydrogen storage materials. Hydrogen storage in a solid material causes repeated volumetric changes and internal stresses during hydrogen entry (hydrogenation) and exit (dehydrogenation). This cyclic stress can lead to pulverization of the material over time, resulting in performance loss. This study demonstrates that all compounds examined meet the Born-Huang criteria, indicating mechanical stability, which is a fundamental requirement for a storage material. However, Pugh ratio and Poisson's ratio analyses reveal that all these materials possess a brittle nature. This brittle structure indicates that the materials may be sensitive to cyclic stress when in bulk form and that engineering strategies such as nano structuring or composite formation may be necessary to manage this mechanical weakness in practical applications. Therefore, the analysis of mechanical properties allows us to anticipate the steps required to transform the high storage capacity of these new materials into a real technology.

3.5. Electronic band structure and density of states

The determination of the electronic band structure is crucial for understanding the essential physical properties of crystal solids, especially regarding their optical response and charge transport mechanisms. The electronic band structures ($E-E_F$) of $LiMH_x$ (M = Sc, Ti, x = 3, 4, 5) compounds were computed along high-symmetry k-paths, as depicted in Figs. 4 (a)-(c) and 5 (a)-(c). For cubic $LiScH_3$ and $LiTiH_3$, the k-paths followed the sequence X- R- M − Γ- R, while for tetragonal $LiScH_{4/5}$ and $LiTiH_{4/5}$, the paths spanned Z- A- M − Γ- Z- R- X- Γ. In these diagrams, the Fermi energy (E_F) is marked by a red dashed horizontal line, serving as a reference for the energy levels. The electronic characteristics of these $LiMH_x$ (M = Sc, Ti, x = 3, 4, 5) compounds offer critical insights into their suitability for hydrogen storage applications. These properties significantly influence the materials' electronic behavior, which in turn affects their thermodynamic stability and hydrogen storage efficiency. The electronic profiles of the investigated

Table 7
The minimum and maximum values of the Young's modulus (GPa), bulk modulus (GPa), shear modulus (GPa), hardness (GPa), and their ratios for $LiMH_x$ (M = Sc, Ti, x = 3, 4, 5) compounds.

Compound	E_{max}	E_{min}	A_E	B_{max}	B_{min}	A_B	G_{max}	G_{min}	A_G	H_{vmax}	H_{vmin}	A_{H_v}
$LiScH_3$	175.59	111.18	0.14	72.56	72.56	0.00	80.05	44.66	0.15	26.14	7.46	0.35
$LiScH_4$	120.04	52.60	0.27	60.38	37.96	0.16	48.76	17.02	0.31	10.11	2.41	0.36
$LiScH_5$	130.68	59.83	0.28	86.12	33.38	0.34	61.96	28.71	0.21	11.83	2.87	0.43
$LiTiH_3$	132.76	75.29	0.18	64.32	64.32	0.00	57.42	29.07	0.18	15.73	2.67	0.51
$LiTiH_4$	128.93	81.48	0.14	72.40	48.28	0.14	52.41	29.52	0.16	13.60,	2.07	0.32
$LiTiH_5$	168.93	103.94	0.12	82.50	55.04	0.14	76.86	35.95	0.14	27.75	3.15	0.38

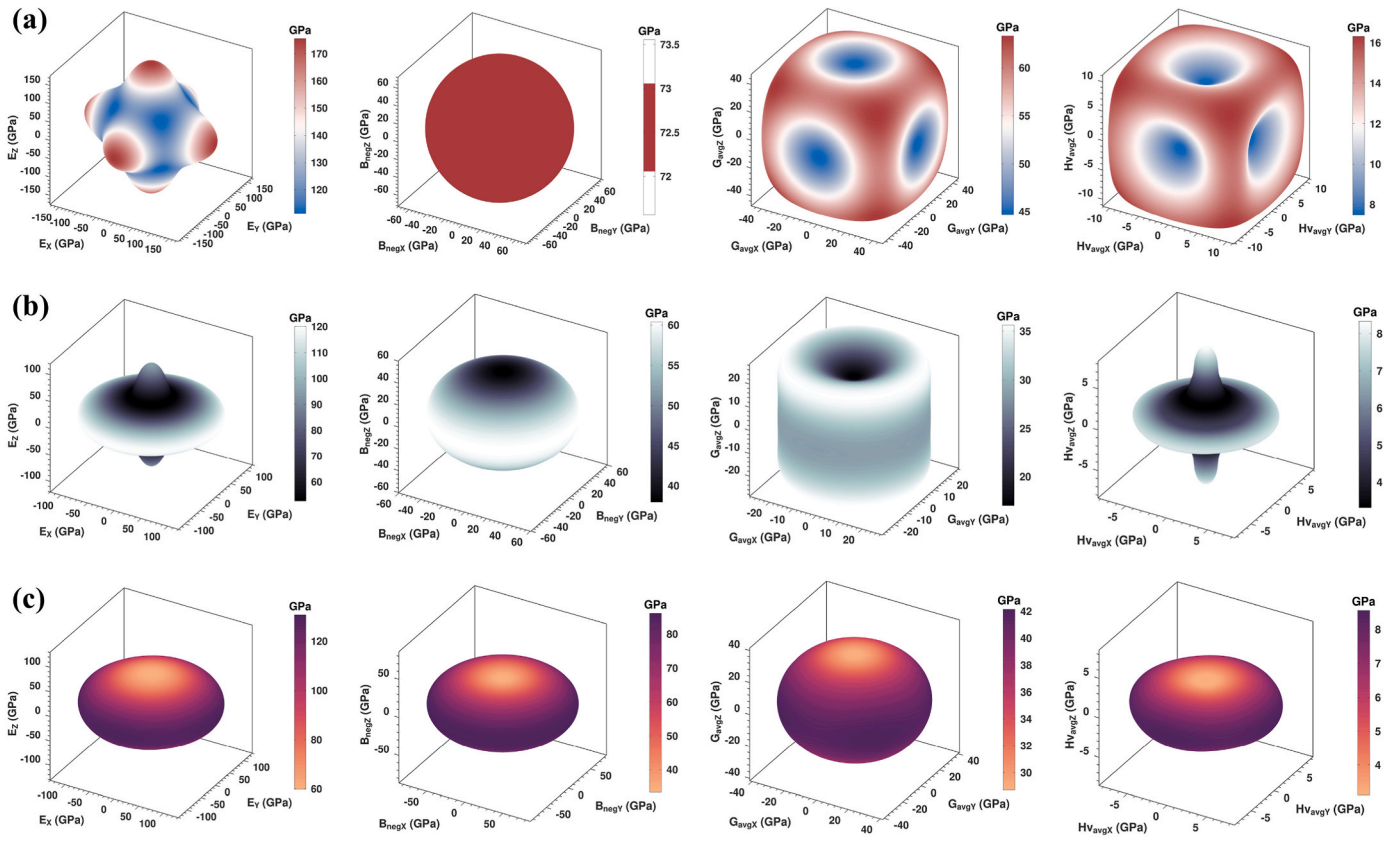

Fig. 2. 3D directional dependence of the shear modulus, bulk modulus, young modulus, hardness for (a) $LiScH_3$, (b) $LiScH_4$, and (c) $LiScH_5$.

compounds reveal a metallic character, as both the conduction and valence bands intersect the Fermi level. This behavior is further elucidated through the total density of states (TDOS) and partial density of states (PDOS) plots for $LiMH_x$ (M = Sc, Ti; x = 3, 4, 5) compounds, which are detailed in Figs. 4 (a)–(c) and 5(a)-(c). For $LiScH_3$, the density of states depicted in Fig. 4(a) highlights that the Sc-3d orbital predominantly contributes to the valence band near the Fermi level, while H-1s orbitals play a significant role from −2 eV to −10 eV. In the conduction band, the Sc-3d orbital dominates near the Fermi level, with contributions from Sc-4s between 4 eV and 6 eV and Li-2s between 6 eV and 8 eV. For $LiScH_4$, as shown in Fig. 4(b), the Sc-3d orbital is the primary contributor to the valence band close to the Fermi level, complemented by H-1s contributions from −1 eV to −10 eV, while the conduction band features dominant Sc-3d input near the Fermi level and Li-2s influence from 6 eV to 8 eV. In the case of $LiScH_5$, Fig. 4(c) indicates that the H-1s orbital is the leading contributor to the valence band, whereas the conduction band is shaped by H-1s near the Fermi level and Sc-3d from 1 eV to 8 eV.

For $LiTiH_3$, the density of states in Fig. 5(a) reveals that the Sc-3d orbital governs the valence band near the Fermi level, with notable H-1s contributions from −3 eV to −9 eV; in the conduction band, Sc-3d dominates near the Fermi level, with Li-2s contributions from 4 eV to 6 eV. Similarly, for $LiTiH_4$, Fig. 5(b) shows the Sc-3d orbital as the primary valence band contributor near the Fermi level, supported by H-1s from −2 eV to −9 eV, while the conduction band is driven by Sc-3d near the Fermi level and Li-2s from 6 eV to 9 eV. For $LiTiH_5$, Fig. 5(c) indicates that the Sc-3d orbital leads the valence band close to the Fermi level, with H-1s contributions from −3 eV to −9 eV, and the conduction band is dominated by Sc-3d near the Fermi level, alongside Li-2s from 6 eV to 9 eV. These observations underscore the evolving roles of metal d-orbitals and hydrogen s-orbitals in shaping the electronic structure as the hydrogen content varies. The analysis indicates that $LiMH_x$ (M = Sc, Ti, x = 3, 4, 5) compounds exhibit hybridization between the d-states of M (Sc, Ti) and the s-states of H near the Fermi level (E_F), resulting in pronounced metallic behavior. Notably, metallic materials are advantageous for hydrogen storage applications due to their high electrical conductivity, which promotes efficient charge transfer during hydrogen absorption and desorption processes [80,81]. Consequently, the metallic nature of these hydrides positions them as promising candidates for hydrogen storage applications [82]. Furthermore, metals typically demonstrate favorable adsorption properties for hydrogen molecules, which can significantly enhance storage capacity [83].

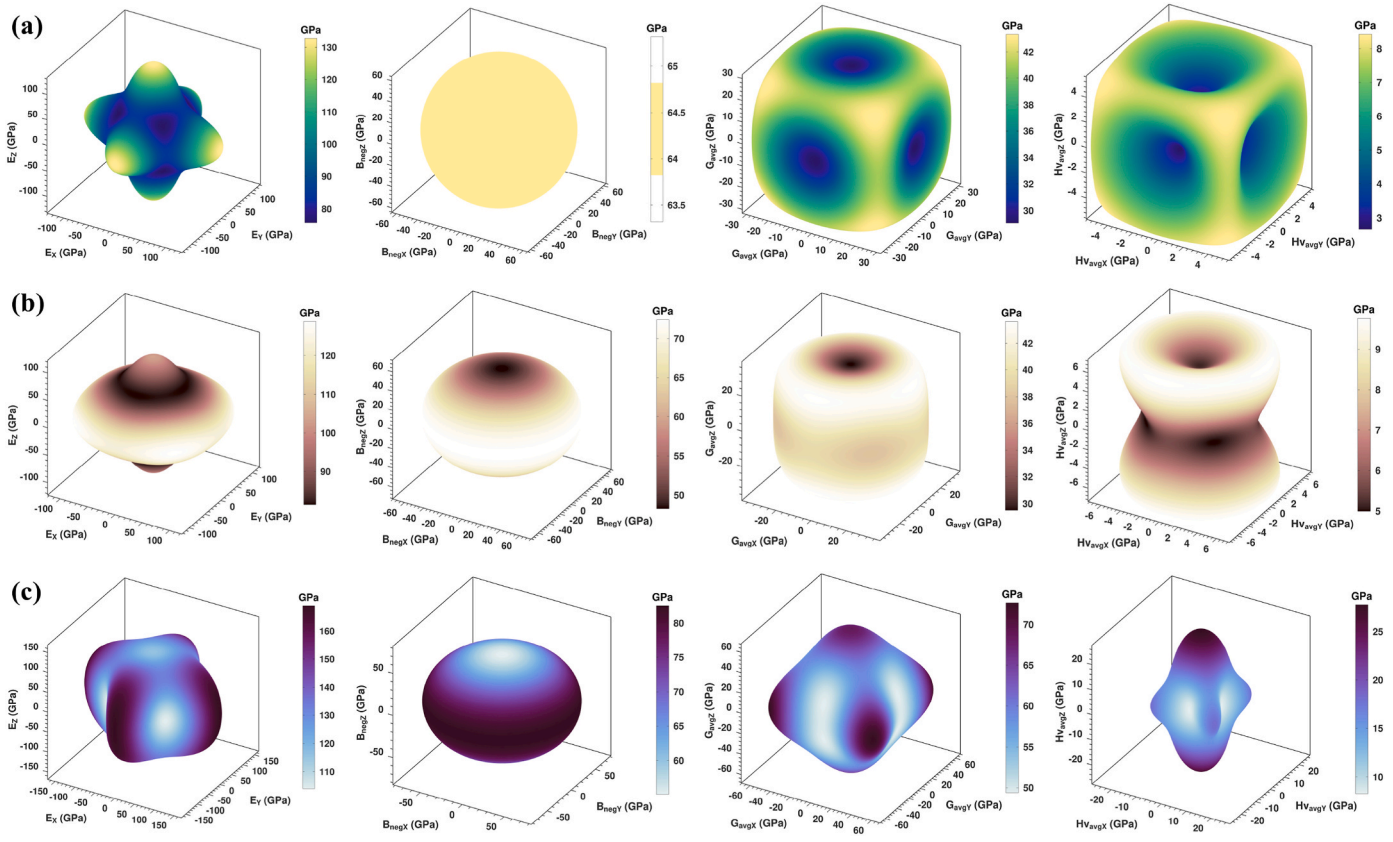

Fig. 3. 3D directional dependence of the shear modulus, bulk modulus, young modulus, hardness for (a) $LiTiH_3$, (b) $LiTiH_4$, and (c) $LiTiH_5$.

3.6. Thermophysical properties

In crystal solids, the Debye temperature (θ_D) emerges as a crucial thermophysical property, intricately connected to an array of physical attributes, including melting temperature, thermal expansion, heat conductivity, lattice dynamics, interatomic bond strength, and phonon-mediated specific heat capacity. This parameter delineates the temperature threshold at which all vibrational modes within the crystal lattice achieve full excitation. At reduced temperatures, thermal excitations predominantly stem from acoustic vibrational modes, establishing θ_D as a vital marker of phonon behavior. The value of θ_D is shaped by the rigidity of the crystal lattice and the masses of its constituent atoms. Materials characterized by robust interatomic forces, elevated melting points, increased hardness, rapid mechanical wave transmission, and lighter average atomic masses typically exhibit higher Debye temperatures. At sufficiently low temperatures, consistency is observed between θ_D values obtained from elastic moduli and those derived from specific heat measurements. In the present investigation, θ_D was determined by leveraging the crystal's density (ρ) and the mean sound velocity (v_m), employing the well-established relation outlined in Ref. [84].

$$\theta_D = \frac{h}{k_B}\left[\left(\frac{3N}{4\pi}\right)\frac{N_A\rho}{M}\right]^{\frac{1}{3}} v_m \tag{29}$$

The Debye temperature (θ_D) is evaluated through a widely recognized formula that integrates fundamental physical constants, including Planck's constant (h), Boltzmann constant (k_B), and Avogadro's number (N_A), with material-specific attributes such as density (ρ), molecular weight (M), number of atoms per unit cell (N), and mean sound velocity (v_m). This investigation underscores a direct correlation between θ_D and v_m, where v_m is fundamentally influenced by the elastic properties inherent to the crystalline structure. The mean sound velocity (v_m) is determined through a quantitative approach involving the bulk modulus, shear modulus, and the longitudinal and transverse sound velocities (v_l and v_t), consistent with the established methodology detailed in Ref. [85].

$$v_t = \sqrt{\frac{G}{\rho}}, v_l = \sqrt{\frac{3B+4G}{3\rho}}, v_m = \left[\frac{1}{3}\left(\frac{2}{v_t^3}+\frac{1}{v_l^3}\right)\right]^{-\frac{1}{3}} \tag{30}$$

The calculated values of θ_D, v_m, v_l, v_t and ρ for $LiMH_x$ (M = Sc, Ti, x = 3, 4, 5) compounds are presented in Table 8. The Debye temperature serves as a critical indicator of bond strength and thermal transport properties, with rising values corresponding to enhanced chemical bonding and superior phonon-mediated thermal conductivity. As evidenced by the tabulated data, the Debye temperature for Sc-based compounds is $LiScH_3 > LiScH_5 > LiScH_4$. The $LiScH_3$ compound, with the highest θ_D value, indicates that the atoms in the crystal lattice have stiffer vibrational modes and therefore exhibit high lattice rigidity. The lowest θ_D value in $LiScH_4$ indicates that the crystal lattice is softer and the moduli of elasticity may be smaller. The pronounced and nonlinear change in θ_D value with increasing hydrogen content ($x = 3 \rightarrow 5$) reveals the influence of H atoms on the lattice dynamics. The value of θ_D for Ti-based compounds tends to increase with hydrogen content. The $LiTiH_5$ compound has the highest Debye temperature with a value of 911.28 K. This indicates that the lattice vibrations occur at high frequencies, and the structure is more mechanically robust.

The increase in θ_D with increasing hydrogen content in Ti-based systems suggests that H atoms strengthen the stiffness of the structure and the bonds become stronger. In summary, the increase in θ_D with increasing hydrogen content in Ti-based systems suggests that H atoms strengthen the stiffness of the structure and the bonds become stronger. While Sc-based systems show more rigid structures at low H content, they lose this advantage with increasing H content. This suggests that Ti–H bonds gain stronger covalent components at high hydrogen concentration and increase the lattice rigidity.

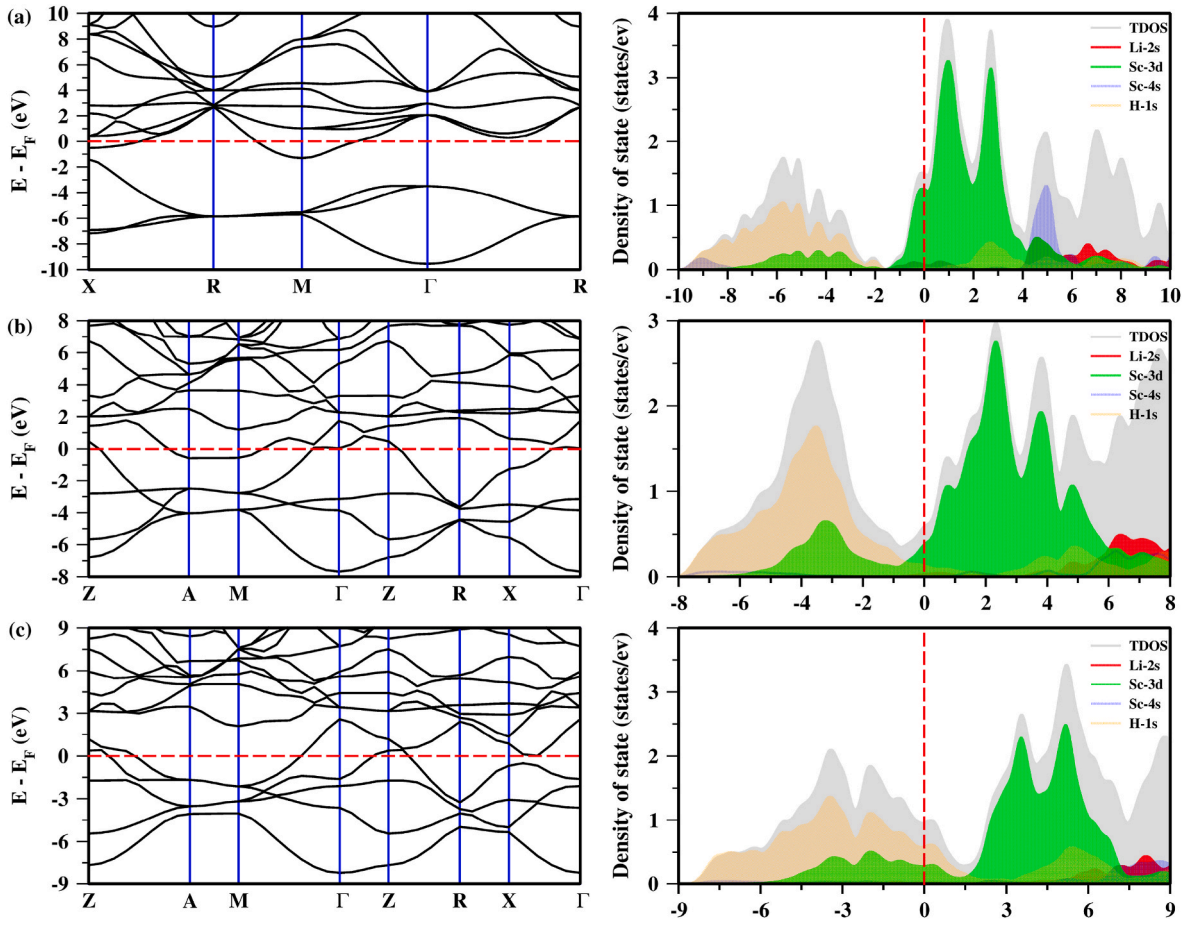

Fig. 4. Energy band structure and density of states of (a) $LiScH_3$, (b) $LiScH_4$ and (c) $LiScH_5$.

A material's thermal performance and practical operational boundaries are fundamentally governed by its melting temperature (T_m). This parameter serves as a vital indicator of thermal stability, intrinsically linked to other fundamental characteristics such as thermal expansion coefficients, elastic moduli, and interatomic bond strengths. Materials possessing elevated melting points typically exhibit more robust interatomic bonding, which in turn correlates with reduced thermal expansion. Precise knowledge of T_m is particularly valuable for defining safe operating temperature ranges, ensuring that materials maintain their structural integrity and functionality without succumbing to oxidative processes, detrimental phase transformations, or thermally induced mechanical failure [86]. In this investigation, we computationally estimated the T_m values by employing a well-established theoretical relationship that correlates elastic properties with melting characteristics, utilizing an analytical formulation derived from fundamental elastic constants [87].

$$T_m = 354 + 1.5(2C_{11} + C_{33}) \tag{31}$$

As presented in Table 8, the calculated melting temperatures for $LiMH_x$ (M = Sc, Ti, x = 3, 4, 5) compounds reveal significant differences in thermal stability between the compounds. Of the Sc-based compounds, $LiScH_3$ has the highest melting temperature, indicating that the compound is the most thermally stable. As the hydrogen content increases ($x = 3 \rightarrow 5$), the T_m value decreases markedly. This indicates that increasing H atoms relax the lattice structure, reducing the bond strength and weakening the thermal stability. The T_m values of $LiScH_4$ and $LiScH_5$ compounds are quite close to each other, suggesting that an equilibrium state is reached due to the effect of high H concentration. The T_m values of Ti based compounds vary in a narrower range and show an increasing trend with increasing hydrogen content. The T_m values of Ti based compounds vary in a narrower range and show an increasing trend with increasing hydrogen content. $LiTiH_5$ has the highest T_m value, indicating that Ti–H bonds become more stable in hydrogen-rich environment, which increases the potential of Ti-based compounds to maintain structural integrity at high temperatures. x = 3, the Sc-based compound ($LiScH_3$) has a higher melting temperature compared to the Ti-based one, suggesting that Sc–H and Sc–Li bonds may be stronger. In the x = 4 and x = 5 cases, Ti-based compounds show higher T_m values, proving that they are more resistant to high hydrogen content. It can be interpreted that Ti–H bonds become more thermally stable as they become saturated with hydrogen. There is a correlation between melting temperature and Debye temperature, and it has been observed that systems with high Tm values generally have high θ_D values. This is related to the lattice rigidity and bond strength of the material. In terms of application area, Ti based compounds are more advantageous especially in high temperature and hydrogen rich conditions.

Assessing the thermal transport characteristics of materials is of paramount importance, particularly when considering their performance in elevated-temperature environments. Within the spectrum of key thermophysical descriptors, the minimum thermal conductivity (K_{min}) stands out as a fundamental metric. It provides a crucial measure of a material's inherent ability to conduct heat, especially under conditions where phonon scattering is maximized. In this investigation, K_{min} values were computationally determined by applying the theoretical framework detailed in Equation (32) [88]. The resultant K_{min} values for the studied materials are systematically compiled and presented in Table 8.

$$K_{min} = k_B v_m \left(\frac{M}{n\rho N_A}\right)^{-\frac{2}{3}} \tag{32}$$

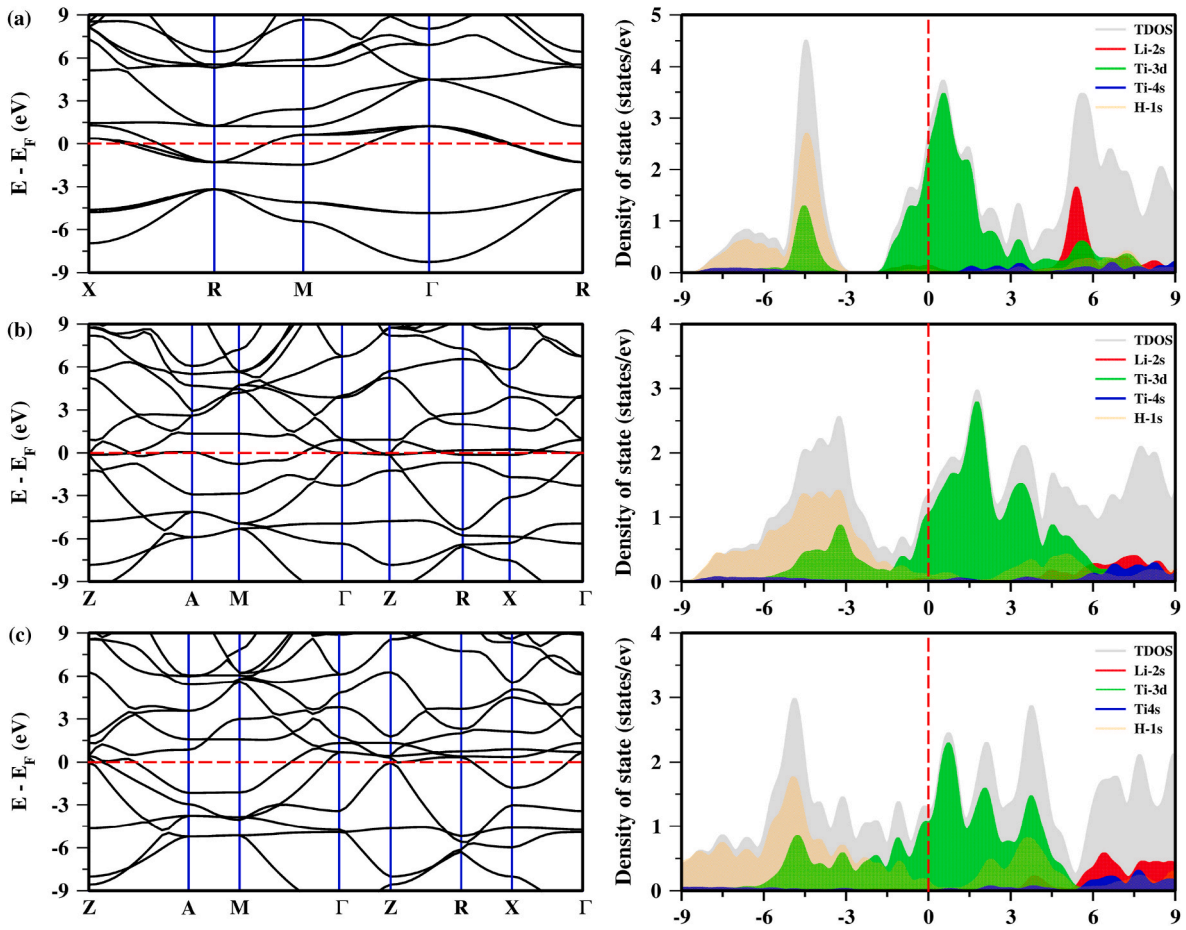

Fig. 5. Energy band structure and density of states of (a) $LiTiH_3$, (b) $LiTiH_4$ and (c) $LiTiH_5$.

Table 8
Calculated mass density (ρ in g/cm^3), longitudinal, transverse, and sound velocities (v_l, v_t, and v_m in m s^{-1}, respectively), Debye temperature (θ_D in K), melting temperature (T_m in K), and minimum thermal conductivity (kmin in Wm^{-1} K^{-1}) of $LiMH_x$ (M = Sc, Ti, x = 3, 4, 5) compounds.

Compound	ρ	v_t	v_l	v_m	T_m	θ_D	K_{min}	γ
$LiScH_3$	2.33	4929.16	7973.39	5436.33	1160.84	814.80	1.90	1.25
$LiScH_4$	1.73	4305.47	7376.77	4775.27	886.81	684.64	1.53	1.46
$LiScH_5$	1.86	4581.00	7720.13	5073.09	905.40	779.78	1.87	1.40
$LiTiH_3$	2.04	4330.62	7515.79	4808.64	987.98	678.34	1.49	1.51
$LiTiH_4$	2.14	4349.80	7383.67	4820.32	934.61	729.75	1.72	1.43
$LiTiH_5$	2.18	5187.10	8282.55	5712.85	1074.95	911.28	2.26	1.20

Minimum thermal conductivity (K_{min}, W/m.K) refers to the lower limit of a material's ability to conduct heat and is directly related to phonon transmission mechanisms, lattice irregularities and atomic bond strengths. $LiScH_4$ has the lowest thermal conductivity, and this structure seems to have reached the highest level in terms of phonon scattering. This indicates that with increasing hydrogen content in the structure of $LiScH_4$, phonon scattering deteriorates, and a more disordered lattice structure is formed. Interestingly, an increase is again observed in $LiScH_5$, which may indicate that the structure becomes more ordered, or the bond rigidity increases. In general, Sc-based systems are advantageous in terms of low heat conduction hydrogen storage materials. $LiTiH_3$ has the lowest K_{min} value, indicating that this compound has structurally more phonon scattering and thus a weaker heat conduction. As the hydrogen content increases (x = 3 → 5), the K_{min} value increases steadily, indicating that the phonon transport capacity of the structure is strengthened. $LiTiH_5$ has the highest minimum thermal conductivity of 2.26 W/m.K. This suggests that the crystal structure is more ordered, and the bonds are more rigid. x = 3, the Ti-based compound has lower thermal conductivity, indicating that the structure contains more phonon scattering. x = 5, the Ti-based structure has significantly better thermal conductivity, suggesting that the orderliness or bond rigidity of the structure is high. In general, Ti-based compounds show an increase in thermal conductivity with increasing hydrogen content, whereas Sc-based compounds show a more disordered trend. Scandium-based compounds, especially in combination with $LiScH_4$, have low thermal conductivity, making them poor conductors of heat, potentially ideal as thermal barriers or hydrogen storage materials. Titanium-based systems become more ordered and phonon transmission increases with increasing hydrogen content. It can be inferred that these structures have a better ability to conduct heat and have a more rigid lattice structure.

The Grüneisen parameter (γ) stands as a fundamental quantity in solid-state physics, serving to characterize the degree of anharmonicity in lattice vibrations and their coupling to a material's thermodynamic properties. This dimensionless parameter establishes a crucial connection between a material's elastic behavior and its thermal response.

Elevated values of γ are directly correlated with increased thermal expansion coefficients, more significant variations in bulk modulus with temperature, and stronger phonon-phonon interaction strengths, collectively indicating greater lattice anharmonicity and more pronounced temperature-dependent phenomena [89].

$$\gamma = \frac{3(1+\nu)}{2(2-3\nu)} \tag{33}$$

Among Sc-based compounds, the Grüneisen parameter increases from x = 3 to x = 4, indicating that anharmonic effects and phonon-phonon scattering increase. Although γ decreases slightly at x = 5, it is still higher than at x = 3. This indicates that the structure becomes more sensitive to phonon expansion with increasing hydrogen content. $LiScH_4$ has the highest γ value among this trio, supporting that it exhibits high anharmonicity and contributes to its low thermal conductivity. In the Ti-based system, γ decreases steadily with increasing hydrogen content. This indicates that the phonon anharmonicity decreases, meaning that the crystal structure becomes more ordered and the phonons more stable. In particular, the $LiTiH_5$ compound has the lowest Grüneisen parameter with γ = 1.20. This indicates that it experiences less phonon scattering, consistent with a high thermal conductivity. At x = 3, the Ti-based compound has a higher γ value, while at x = 5 the situation is reversed. This suggests that Ti-based systems become more stable and ordered as the hydrogen content increases, while the anharmonicity remains more stable in Sc systems. These results are in agreement with other parameters such as the minimum thermal conductivity and the Debye temperature and provide a holistic structural-photonic understanding. The findings in this section are completely new and there is no comparable data in the literature.

3.7. Optical properties

The optical properties of materials provide critical insights into their electronic structure, atomic bonding, and fundamental excitation mechanisms. This section presents and interprets the calculated spectra of dielectric function, refractive index, absorption coefficient, reflectivity, optical conductivity, and energy loss function for the $LiTiH_x$ and $LiScH_x$ (x = 3, 4, 5) series of compounds. Figs. 6 and 7 display the calculated optical spectra for the $LiScH_x$ and $LiTiH_x$ (x = 3, 4, 5) compounds, respectively.

The dielectric function $\varepsilon(\omega) = \varepsilon_1(\omega) + i\varepsilon_2(\omega)$, is a fundamental property that describes how a material responds to an external electromagnetic field. The real part (ε_1) represents the polarizability of the material, while the imaginary part (ε_2) accounts for absorption and energy dissipation. Fig. 6 (a)–(c) presents the dielectric function for the $LiScH_x$ (x = 3, 4, 5) series. The trend in the static dielectric constant for $LiScH_x$ (x = 3, 4, 5) is more complex: 16.99 for $LiScH_3$, 7.21 for $LiScH_4$, and 44.69 for $LiScH_5$. The notable decrease for $LiScH_4$ indicates that its electronic structure differs significantly from the others. The graph shows peaks in ε1(ω) around the 5–10 eV range. The value of $\varepsilon_1(\omega)$ at 0 eV $\varepsilon_1(0)$ is very high for $LiScH_5$ (44.69), strongly indicating high polarizability and metallic-like behavior for this compound. The onset of $\varepsilon_2(\omega)$ suggests a band gap for $LiScH_3$ and $LiScH_4$, whereas for $LiScH_5$, it starts from 0 eV (or very low energy), indicating a metallic character.

As shown in Fig. 7 (a)–(c), the static dielectric constant $\varepsilon_1(0)$ for the $LiTiH_x$ (x = 3, 4, 5) series significantly increases with increasing hydrogen concentration: 6.32, 15.30, and 44.69 for x = 3,4, and 5, respectively. This increase suggests an enhanced overall polarizability and a tendency towards a more metallic-like character with higher H content. The peaks in $\varepsilon_1(\omega)$ indicate strong polarization resonances at specific photon energies. For $LiTiH_3$, a peak is observed around 4.74 eV, while for higher H content compounds, these peaks shift towards higher

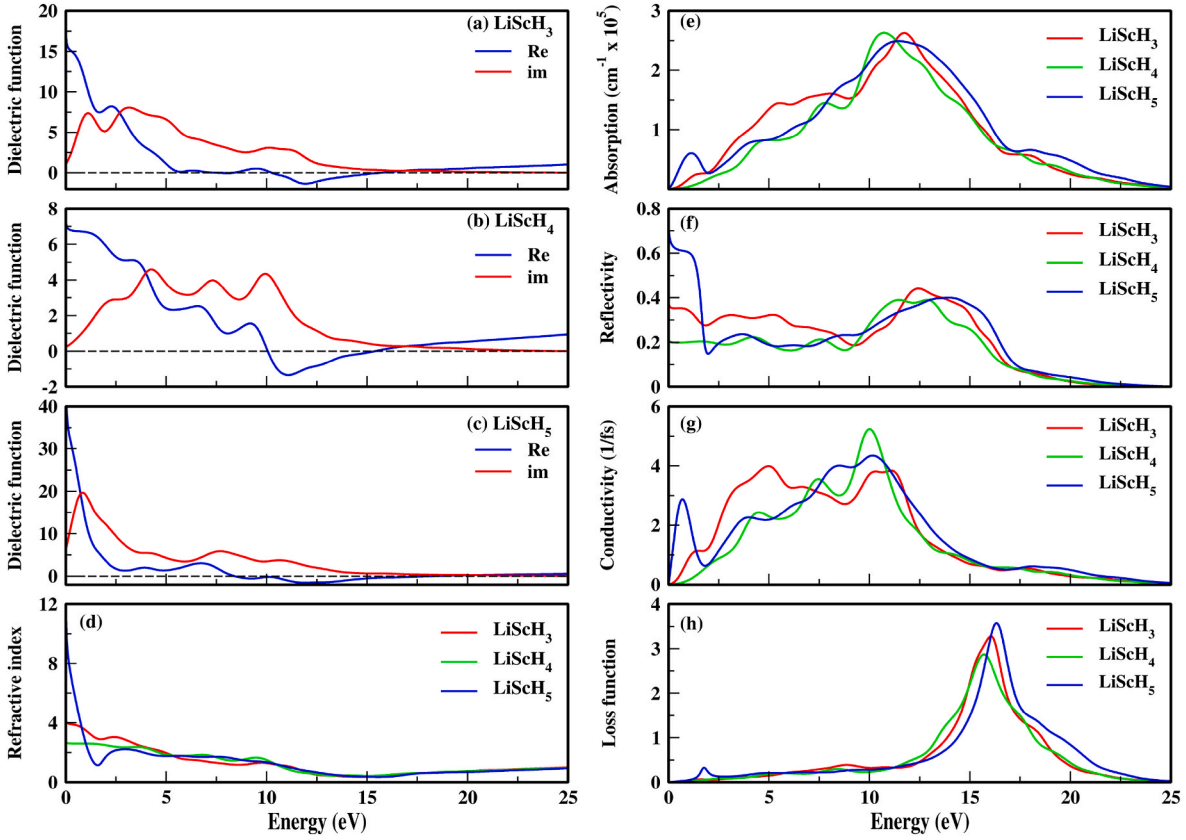

Fig. 6. Optical properties of $LiScH_x$ (x = 3, 4, 5) compounds. (a)–(c) Dielectric function, (d) Refractive index, (e) Absorption, (f) Reflectivity, (g) Conductivity and (h) Loss function.

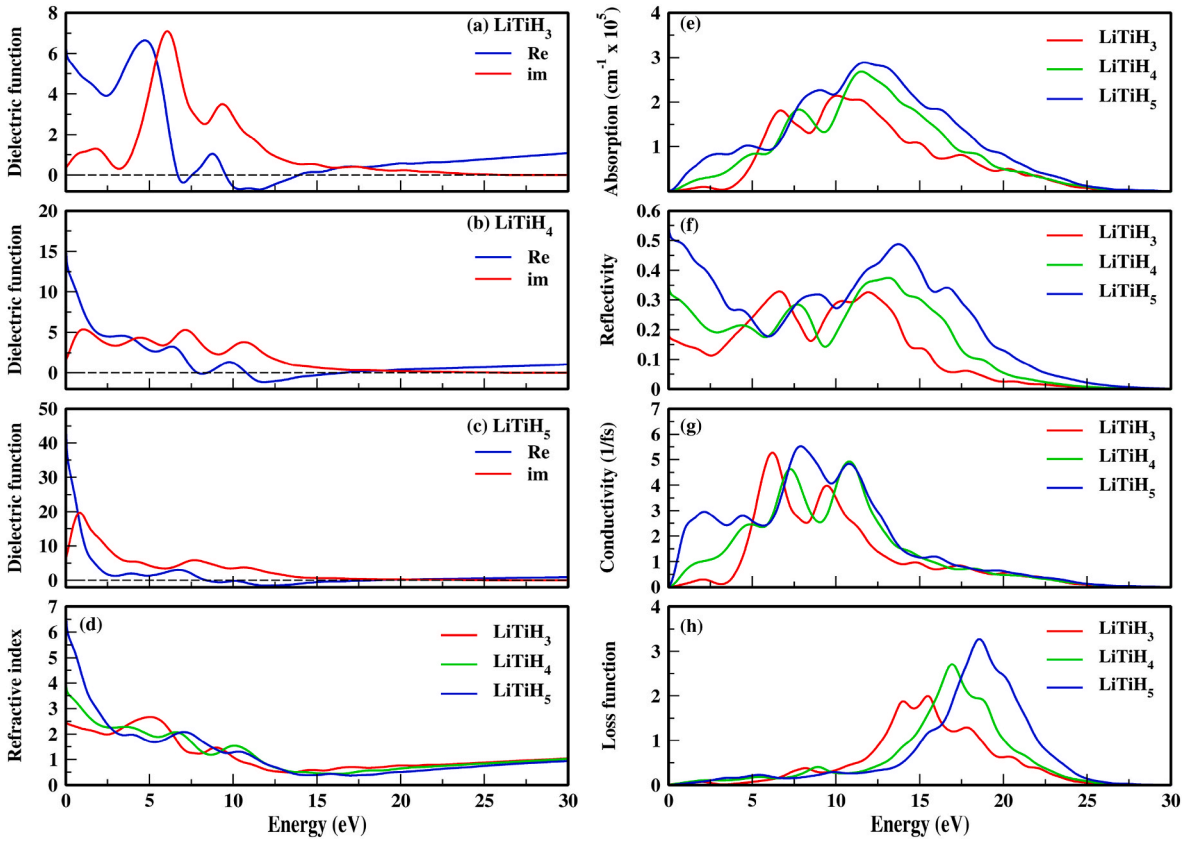

Fig. 7. Optical properties of $LiTiH_x$ (x = 3, 4, 5) compounds. (a)–(c) Dielectric function, (d) Refractive index, (e) Absorption, (f) Reflectivity, (g) Conductivity and (h) Loss function.

energies. The energy at which $\varepsilon_2(\omega)$ becomes non-zero signifies the optical band gap or the minimum energy for electronic transitions. For the $LiTiH_x$ series, this onset appears to shift to lower energies as H concentration increases, suggesting a narrowing of the optical band gap.

The refractive index n(ω) describes the material's ability to bend light and is related to $\epsilon 1(\omega)$. Figs. 6(d) and 7(d) show the refractive index spectra for $LiScH_x$ and $LiTiH_x$ (x = 3, 4, 5). The refractive index values in the low-energy limit (0 eV) are consistent with the square root of the static dielectric constant. For $LiTiH_x$, n(0) values increase as 2.51, 3.92, and 6.70. For $LiScH_x$, they follow the trend 4.12, 2.68, and 11.34. The exceptionally high refractive index of $LiScH_5$ at 0 eV (11.34) indicates a strong response in the optical range. Peaks in the refractive index spectra reflect the resonances in the dielectric function, indicating strong light interaction at those specific energies.

The absorption coefficient α(ω) quantifies how efficiently light is absorbed by the material. The spectra in Figs. 6(e) and 7(e) show that absorption is generally strong in the ultraviolet (UV) energy range for both series. For LiTiHx, the onset of absorption tends to shift to lower energies with increasing H concentration. The energies and intensities of the absorption peaks vary with H concentration: 2.14×10^5 cm^{-1} at 10.11 eV for $LiTiH_3$, 2.68×10^5 cm^{-1} at 11.51 eV for $LiTiH_4$, and 2.89×10^5 cm^{-1} at 11.73 eV for $LiTiH_5$. This indicates that the maximum absorption intensity increases with increasing H content.

For the $LiScH_x$ series, the onset of absorption indicates a band gap in $LiScH_3$ and $LiScH_4$, while it begins at lower energies in $LiScH_5$. The absorption peak values are given as 2.63×10^5 cm^{-1} at 11.72 eV for $LiScH_3$, 2.63×10^5 cm^{-1} at 10.71 eV for $LiScH_4$, and 2.49×10^5 cm^{-1} at 11.44 eV for $LiScH_5$. The peak intensities are of similar magnitude for all three $LiScH_x$ compounds, but the peak energies show some variation. The strong absorption in the UV region for both $LiTiH_x$ and $LiScH_x$ series suggests the potential of these materials for harvesting photons in this energy range, which could be relevant for applications like photocatalytic hydrogen production.

Reflectivity R(ω) defines the fraction of incident light reflected from the material surface. Figs. 6 (f) and 7 (f) show the reflectivity spectra for both series. The reflectivity value in the low-energy limit (0 eV) is related to the high refractive index and dielectric constant values. For $LiTiH_x$, the reflectivity at 0 eV increases with H concentration (up to 0.55 for $LiTiH_5$). For $LiScH_x$, the reflectivity at 0 eV follows the trend of $\varepsilon_1(0)$: lower values for $LiScH_3$ and $LiScH_4$, and a considerably high value (0.71) for $LiScH_5$. The particularly high low-energy reflectivity of $LiScH_5$ suggests metallic-like surface properties. Peaks in the reflectivity spectra correspond to resonance regions in the dielectric function, and significant reflectivity is observed in the UV energy range for both series (0.33 at 6.40 eV for $LiTiH_3$, 0.38 at 13.11 eV for $LiTiH_4$; 0.44 at 12.44 eV for $LiScH_3$, 0.39 at 12.87 eV for $LiScH_4$).

The optical conductivity σ(ω) characterizes the material's response to an optical field in terms of charge carrier motion. The spectra in Figs. 6(g) and 7(g) show that optical conductivity typically starts above certain energy thresholds, which are related to the material's band gap. For $LiTiH_x$, the peaks in optical conductivity are at 6.19 eV with a value of 5.27 for $LiTiH_3$, 7.28 eV with 4.63 for $LiTiH_4$, and 7.88 eV with 5.52 for $LiTiH_5$. The peak positions shift to higher energies with increasing H, while the peak intensities are similar.

The values of the $LiScH_x$ series starting from zero eV show its metallic character. The peak conductivity values are observed at 4.98 eV with 3.99 for $LiScH_3$, 10 eV with 5.24 for $LiScH_4$, and 10.15 eV with 4.34 for $LiScH_5$. The peak positions for $LiScH_4$ and $LiScH_5$ are close to each other and at higher energies compared to $LiScH_3$. The significant conductivity of $LiScH_5$ at low energies further supports its metallic-like or narrow band gap structure.

The energy loss function, L(ω), describes the probability that a fast electron traversing the material will lose energy. Peaks in L(ω) typically correspond to plasma oscillations (plasmons) of the electron gas. The

main plasmon peaks are located in the high-energy range (15–20 eV), as shown in Figs. 6(h) and 7(h). For $LiTiH_x$, the plasmon peaks shift to higher energies and their intensity increases with increasing H concentration: 1.99 at 15.49 eV for $LiTiH_3$, 2.71 at 16.93 eV for $LiTiH_4$, and 3.27 at 18.56 eV for $LiTiH_5$. This could be associated with an increase in free carrier density with higher H content. For the $LiScH_x$ series, the plasmon peaks are observed at 16.06 eV with 3.28 for $LiScH_3$, 15.70 eV with 2.87 for $LiScH_4$, and 16.34 eV with 5.74 for $LiScH_5$. While the peak positions do not show as pronounced an energy shift as in $LiTiH_x$, the intensity of the plasmon peak for $LiScH_5$ is significantly higher compared to other $LiScH_x$ and $LiTiH_x$ compounds. This strongly suggests the presence of a higher free electron density or a different plasmon resonance mechanism in $LiScH_5$.

The comparative analysis of the optical properties of $LiTiH_x$ and $LiScH_x$ compounds reveals both similarities and significant differences in their electronic structures and optical responses. In both series, variations in H concentration dramatically affect their dielectric properties, metallic character, and high-energy plasmonic responses. Specifically, the high static dielectric constants, high low-energy reflectivity, and pronounced plasmon peak (especially for $LiScH_5$) of $LiTiH_5$ and $LiScH_5$ strongly suggest a more metallic-like character for these compounds. Metallic or semi-metallic hydrides are of great interest as potential hydrogen storage materials due to their favorable electronic structures for hydrogen absorption and desorption mechanisms. High reflectivity in certain ranges might also be relevant for thermal management in hydrogen storage systems. The nature of electronic transitions (seen in absorption/conductivity) relates to the types of bonds formed with hydrogen. Overall, the diverse optical responses exhibited by the $LiTiH_x$ and $LiScH_x$ series as a function of H concentration demonstrate that their electronic structures can be sensitively tuned by hydrogen incorporation. This tunability makes these materials potential candidates not only for fundamental scientific research but also for the design of materials with specific functional properties in areas such as hydrogen storage, optoelectronics, and catalysis. Particularly, the extreme dielectric and reflectivity properties of $LiScH_5$ open new avenues for understanding the optical behavior of metallic hydrides and their potential for high-density hydrogen storage applications.

The optical properties presented in this section provide in-depth information about the material's electronic structure, shedding light on its indirect but significant relationship with hydrogen storage performance, particularly with kinetic processes. A material's hydrogen absorption and desorption rate (kinetics) is largely governed by its electronic structure. In this study, both electronic band structure analyses and the interpretation of optical spectra confirmed that all $LiMH_x$ compounds examined possess a metallic character. The metallic structure is quite advantageous for hydrogen storage kinetics; because the presence of free electrons can catalyze the dissociation of H_2 molecules on the surface and facilitate the rapid transport (diffusion) of hydrogen ions (H^+) and electrons within the lattice. In this study, the high static dielectric constant and pronounced reflectivity at low energies observed for compounds such as $LiScH_5$ and $LiTiH_5$, in particular, are indicative of this beneficial metallic nature. Consequently, the analysis of optical properties provides strong evidence that these new hydrides may potentially possess fast hydrogen uptake/desorption kinetics.

Combining these optical characterization findings with further theoretical and experimental studies on the electronic and structural properties of these materials will help to fully unlock their potential for various technological applications, including hydrogen storage technologies.

3.8. Hydrogen storage properties

Carbon emissions from fossil fuels and the need for sustainable energy increase the importance of hydrogen as a clean energy carrier. Storing hydrogen safely and efficiently is a key challenge in the transformation of energy infrastructure. In recent years, parallel hydrogen storage systems and especially solid-state storage technologies have attracted considerable attention. These technologies offer the advantages of higher energy density, low risk of leakage and safe transportation. Metal hydrides stand out due to their high gravimetric and volumetric storage capacities, low operating pressure and safety advantages [90]. In addition, next generation solid-state hydrogen storage materials, such as perovskite-type hydrides, are promising with high hydrogen capacity and low dehydrogenation barriers. Recent studies show that perovskite hydrides enriched with light elements have high storage capacity and stable structure [91,92]. Parallel storage systems aim to increase total storage capacity and system security by integrating different materials and technologies [93]. Thanks to all these developments, hydrogen can be used more effectively and safely in mobile applications and fuel cell energy systems [94]. In this study, we carefully examine how well $LiMH_x$ (M = Sc, Ti, x = 3, 4, 5) compounds can store hydrogen. Our analysis covers both the amount of hydrogen these materials can hold by weight ($C_{wt\%}$) and by volume (C_v). To measure the gravimetric hydrogen content, we use the following equation:

$$C_{wt\%} = \left(\frac{\left(\frac{H}{M}\right) M_H}{M_{Host} + \left(\frac{H}{M}\right) M_H} x\,100 \right)\% \tag{34}$$

Table 9 reveals that the gravimetric and volumetric hydrogen storage capacities of $LiMH_x$ (M = Sc, Ti, x = 3, 4, 5) hydrides are highly dependent on their composition. Among the Sc-based compounds studied, LiScH5 stands out with a gravimetric capacity of 8.85 wt% and a volumetric capacity of 163.24 gH_2l^{-1}, significantly outperforming both $LiScH_4$ (7.21 wt%, 123.64 gH_2l^{-1}) and $LiScH_3$ (5.51 wt%, 127.08 gH_2l^{-1}). A similar trend is observed in the Ti-based compounds: $LiTiH_5$ demonstrates superior storage performance, with 8.42 wt% gravimetric and 182.34 gH_2l^{-1} volumetric capacity, surpassing $LiTiH_4$ (6.85 wt%, 145.49 gH_2l^{-1}) and $LiTiH_3$ (5.25 wt%, 105.89 gH_2l^{-1}) by a considerable margin. Notably, all compounds investigated in this study exceed the U. S. Department of Energy's 2025 target of 5.5 wt% for gravimetric capacity, as well as the DOE criterion of gH_2l^{-1} for volumetric capacity by a substantial degree. In particular, $LiTiH_5$ compound has high hydrogen storage capacity compared to many metal hydride compounds reported in the literature with 8.42 Cwt% and 182.34 gH_2l^{-1} C_v [95,96]. To place the hydrogen storage performance of the $LiMH_x$ (M = Sc, Ti; x = 3, 4, 5) compounds examined in this study in a broader context, the calculated gravimetric capacities were compared with those reported in the literature for other complex hydride systems. For example, for X_2CaTiH_6 (X = Li, Na) [97]compounds, the values are 5.3 wt% and 4.14 wt%, for MgX_3H_8 (X = V, Fe) [98] they are 4.14 wt% and 3.84 wt%, for the LiX_3H_8 (X = Ni, Mn, Fe, Cr) [99,100] family they range from 4.23 wt% to 4.71 wt%, 3.47 wt% to 4.03 wt% for XCo_3H_8 (X = Li, Na, K) [101], and 3.72 wt% to 6.16 wt% for X_2MgTiH_6 (X = Li, Na, K) [102]. Compared to these values, all $LiMH_x$ compounds examined in our study (lowest 5.23 % - $LiTiH_3$) have a gravimetric capacity that is higher than or comparable to the vast majority of these systems. In particular, the compounds $LiScH_4$ (7.21 %), $LiTiH_4$ (6.85 %), $LiTiH_5$ (8.42 %), and $LiScH_5$ (8.85 %) offer significantly higher hydrogen storage capacities than all of these compared hydrides. This clearly demonstrates the promising potential of

Table 9
Hydrogen storage performance metrics: theoretical desorption temperature (T_{des}), gravimetric capacity ($C_{wt\%}$), and volumetric capacity (C_v) for $LiMH_x$ (M = Sc, Ti, x = 3, 4, 5) hydrides.

Compound	T_{des}	$C_{wt\%}$	C_v
$LiScH_3$	281.16	5.51	127.08
$LiScH_4$	335.99	7.21	123.64
$LiScH_5$	189.98	8.85	163.24
$LiTiH_3$	152.55	5.23	105.89
$LiTiH_4$	217.94	6.85	145.49
$LiTiH_5$	141.14	8.42	182.34

this new class of materials, discovered using AI-assisted methods, for solid-state hydrogen storage applications.

The hydrogen desorption temperature (T_{des}) represents a pivotal parameter for evaluating the practical viability of solid-state hydrogen storage media. This critical metric, which dictates the temperature at which hydrogen is released from the material, is thermodynamically determined by the ratio of the enthalpy change (ΔH) to the entropy change (ΔS) associated with the dissociation process, as defined by the relationship $T_{des} = \Delta H/\Delta S$. The enthalpy of formation (ΔH) is derived from our calculations based on Equation (8). For typical metal hydride systems, the entropy change (ΔS) is predominantly governed by the liberation of gaseous hydrogen; under standard conditions, this value is widely accepted as approximately −130.7 J/mol.K [103]. Our calculations yielded distinct desorption temperatures for the investigated hydrides. For the Sc-based compounds, we found T_{des} values of 281.16 K for $LiScH_3$, 335.99 K for $LiScH_4$, and 189.98 K for $LiScH_5$. The Ti-based hydrides exhibited lower desorption temperatures, specifically 152.55 K for $LiTiH_3$, 217.94 K for $LiTiH_4$, and 141.14 K for $LiTiH_5$. A comparative analysis of these values against the optimal operating range (233–333 K) targeted by the US Department of Energy for 2025 hydrogen storage systems [104] reveals that $LiScH_3$ and $LiScH_4$ fall within this desirable window.

To assess the practical applicability of our calculated desorption temperatures, it would be illuminating to compare these values with those reported in the literature for other perovskite and complex hydride systems. For example, some hydrides such as $RbXH_3$ (X = Cr, Zr) exhibit quite high desorption temperatures of 545.11 K and 548.15 K, respectively [105]; these values are well above the operational range targeted for most mobile applications. In contrast, the compounds in our study are quite competitive with systems that have more suitable T_{des} values. The $BaXH_3$ (X = Tc, Ta, Mo) family in the literature has desorption temperatures between 217 K and 267 K [30], while LiX_3H_8 (X = Fe, Cr) compounds have desorption temperatures between 322 K and 333 K [100]. These ranges largely overlap with the 233–333 K range targeted by the US Department of Energy. In this context, the desorption temperature of $LiScH_4$ (335.99 K), one of the most promising candidates in our study, is almost identical to that of the high-performance $LiFe_3H_8$ (332.9 K). Similarly, our compounds $LiScH_3$ (281.16 K) and $LiTiH_4$ (217.94 K) also offer T_{des} values suitable for the practical operating range, comparable to $BaTaH_3$ (266.5 K) and $BaMoH_3$ (217.0 K), respectively. Furthermore, some of our compounds, such as $LiTiH_5$ (141.14 K), have lower T_{des} values than these compared systems, offering potential for specialized applications requiring hydrogen release at lower temperatures. This comparison clearly demonstrates how competitive and promising the proposed $LiMH_x$ hydrides are, particularly in terms of the operational temperature targets set by the DOE.

All compounds in our study are notable for both high hydrogen capacity and favorable desorption temperature. $LiScH_4$ presents a balanced structure both by weight and kinetically with a desorption temperature of 335.99 K and a $C_{wt\%}$ of 7.21 %. $LiTiH_5$ stands out as versatile with low temperature release (141.14 K), high $C_{wt\%}$ (8.42 %) and high C_v (182.34 gH_2l^{-1}). These compounds are largely in line with DOE 2025 targets and show a competitive hydrogen storage performance compared to similar systems in the literature.

4. Conclusion

This study has leveraged cutting-edge AI-based autoregressive large language modeling for the generation of novel $LiMH_x$ (M = Sc, Ti; x = 3, 4, 5) hydride structures, followed by a comprehensive first-principles investigation using density functional theory to elucidate their potential for next-generation hydrogen storage and other critical properties. Our rigorous computational analysis has provided detailed insights into their structural, thermodynamic, mechanical, electronic, thermophysical, and optical characteristics. The findings confirm that these AI-predicted compounds exhibit remarkable thermodynamic stability, as evidenced by consistently negative enthalpies of formation, ranging from −0.1912 to −0.4551 eV/atom, coupled with positive cohesive energies. Mechanical stability is also robustly demonstrated through the Born-Huang criteria across all investigated stoichiometries. While $LiTiH_5$ showed the highest hardness of 11.51 GPa, a general brittle behavior was observed for all compounds, a common characteristic in many high-capacity hydride materials. Electronically, all $LiMH_x$ compounds are predicted to possess a metallic nature. Thermophysical analysis provided critical data on their thermal behavior, with Debye temperatures spanning from a low of 684.64 K for $LiScH_4$ to a high of 911.28 K for $LiTiH_5$, offering insights into their vibrational properties and thermal conductivities. Most significantly, the hydrogen storage performance of these materials is highly compelling. $LiScH_4$ stands out, achieving an outstanding gravimetric hydrogen storage capacity of 7.21 wt%, complemented by a high bulk density of 123.64 gH_2/L and a favorable desorption temperature of 335.99 K. These collective properties rigorously demonstrate that $LiScH_4$ specifically meets, and in some aspects exceeds, the stringent gravimetric and volumetric targets established by the U.S. Department of Energy (DOE) for solid-state hydrogen storage materials. Additionally, other compositions such as $LiScH_3$ (5.61 wt%) and $LiTiH_3$ (5.22 wt%) also exhibit gravimetric capacities that align closely with, or surpass, current material-level DOE objectives, positioning them as highly promising candidates.

In conclusion, this work not only provides a foundational understanding of the physical properties of an entirely new set of $LiMH_x$ hydrides but also underscores the transformative power of AI-assisted methodologies in accelerating materials discovery. The exceptional hydrogen storage characteristics, particularly for $LiScH_4$, highlight the immense potential of these lithium-based complex hydrides to address current energy storage challenges. These comprehensive theoretical findings establish an indispensable guide for future experimental synthesis and characterization efforts, paving the way for the development of next-generation solid-state hydrogen storage systems.

CRediT authorship contribution statement

Çağatay Yamçıçır: Writing – review & editing, Writing – original draft, Visualization, Validation, Supervision, Software, Methodology, Investigation, Formal analysis, Data curation, Conceptualization. **Sümeyra Yamçıçır:** Writing – review & editing, Writing – original draft, Resources, Methodology, Conceptualization. **Cihan Kürkçü:** Writing – review & editing, Writing – original draft, Methodology, Formal analysis, Conceptualization.

Informed consent

This article does not contain any studies with human participants performed by any of the authors.

Declaration of generative AI and AI-assisted technologies in the writing process

During the preparation of this work, the author(s) used artificial intelligence to improve the language and readability of the work. After using these AI-assisted applications, the author(s) have revised and edited the content as necessary and take full responsibility for the content of the publication.

Funding

Not Applicable.

Declaration of competing interest

The authors declare that they have no known competing financial interests or personal relationships that could have appeared to influence

the work reported in this paper.

Acknowledgement

This study was supported by the Osmaniye Korkut Ata University under Scientific Research Project No: OKÜBAP 2024-PT1-014.

References

[1] Adewumi A, Olu-lawal KA, Okoli CE, Usman FO, Usiagu GS. Sustainable energy solutions and climate change: a policy review of emerging trends and global responses. World J Adv Res Rev 2024;21:408–20. https://doi.org/10.30574/wjarr.2024.21.2.0474.
[2] Dincer I, Acar C. A review on clean energy solutions for better sustainability. Int J Energy Res 2015;39:585–606. https://doi.org/10.1002/er.3329.
[3] Lakhouit A, Alhathlaul N, El Mokhi C, Hachimi H. Assessing the environmental impact of PV emissions and sustainability challenges. Sustainability 2025;17. https://doi.org/10.3390/su17072842.
[4] Hydrogen factsheet | center for sustainable systems n.d. https://css.umich.edu/publications/factsheets/energy/hydrogen-factsheet (accessed May 21, 2025).
[5] Habib MA, Abdulrahman GAQ, Alquaity ABS, Qasem NAA. Hydrogen combustion, production, and applications: a review. Alex Eng J 2024;100:182–207. https://doi.org/10.1016/j.aej.2024.05.030.
[6] Li R, Kawanami H. A recent review of primary hydrogen carriers, hydrogen production methods, and applications. Catalysts 2023;13. https://doi.org/10.3390/catal13030562.
[7] Akpasi SO, Smarte Anekwe IM, Tetteh EK, Amune UO, Mustapha SI, Kiambi SL. Hydrogen as a clean energy carrier: advancements, challenges, and its role in a sustainable energy future. Clean Energy 2025;9:52–88. https://doi.org/10.1093/ce/zkae112.
[8] Renewable hydrogen - European commission n.d. https://energy.ec.europa.eu/topics/eus-energy-system/hydrogen/renewable-hydrogen_en (accessed May 21, 2025).
[9] Moorthy CB. A concise review of hydrogen production from renewable energy sources with focus on solar, wind, tidal, geothermal, and biomass. Power Syst Technol 2025;49:365–95. https://doi.org/10.52783/pst.1547.
[10] Mekonnin AS, Wacławiak K, Humayun M, Zhang S, Ullah H. Hydrogen storage technology, and its challenges: a review. Catalysts 2025;15:260. https://doi.org/10.3390/catal15030260.
[11] Cekerevac Z, Dvorak Z, Cekerevac D. Logistical challenges in hydrogen supply chain for automotive applications. MEST Journal 2025;13:49–65. https://doi.org/10.12709/mest.13.13.SP.03.
[12] Cousins K, Zhang R. Highly porous organic polymers for hydrogen fuel storage. Polymers 2019;11:690. https://doi.org/10.3390/polym11040690.
[13] da Silva CT, Dias BM de A, Araújo RE, Pellini EL, Laganá AAM. Battery model identification approach for electric forklift application. Energies 2021;14:6221. https://doi.org/10.3390/en14196221.
[14] Zheng J, Wang C-G, Zhou H, Ye E, Xu J, Li Z, et al. Current research trends and perspectives on solid-state nanomaterials in hydrogen storage. Research 2021;2021:3750689. https://doi.org/10.34133/2021/3750689.
[15] Lee J-H, Park J-H, Soon A. Assessing the influence of van der Waals corrected exchange-correlation functionals on the anisotropic mechanical properties of coinage metals. Phys Rev B 2016;94:024108. https://doi.org/10.1103/PhysRevB.94.024108.
[16] Yang X, Li Y, Liu Y, Li Q, Yang T, Jia H. Crystal structure prediction and performance assessment of hydrogen storage materials: insights from computational materials science. Energies 2024;17:3591. https://doi.org/10.3390/en17143591.
[17] Gebretatios AG, Banat F, Cheng CK. A critical review of hydrogen storage: toward the nanoconfinement of complex hydrides from the synthesis and characterization perspectives. Sustain Energy Fuels 2024;8:5091–130. https://doi.org/10.1039/D4SE00353E.
[18] Cao Z, Ouyang L, Wang H, Liu J, Felderhoff M, Zhu M. Reversible hydrogen storage in yttrium aluminum hydride. J Mater Chem A 2017;5:6042–6. https://doi.org/10.1039/C6TA10928D.
[19] Metal hydride storage materials. EnergyGov n.d. https://www.energy.gov/eere/fuelcells/metal-hydride-storage-materials (accessed May 21, 2025).
[20] Yang X, Li Y, Liu Y, Li Q, Yang T, Jia H. Crystal structure prediction and performance assessment of hydrogen storage materials: insights from computational materials science. Energies 2024;17:3591. https://doi.org/10.3390/en17143591.
[21] Metal hydride storage materials. EnergyGov n.d. https://www.energy.gov/eere/fuelcells/metal-hydride-storage-materials (accessed May 21, 2025).
[22] Shah SFA, Murtaza G, Ismail K, Raza HH, Khan IJ. First principles investigation of transition metal hydrides LiXH3 (X = Ti, Mn, and Cu) for hydrogen storage. J Comput Electr 2023;22:921–9. https://doi.org/10.1007/s10825-023-02065-1.
[23] Siddique A, Khalil A, Almutairi BS, Bilal Tahir M, Ahsan T, Hannan A, et al. Structural, electronic, mechanical and dynamical stability properties of LiAH3 (A = Sc, Ti & V) perovskite-type hydrides: a first principle study. Chem Phys 2023;568:111851. https://doi.org/10.1016/j.chemphys.2023.111851.
[24] Shah SFA, Murtaza G, Ismail K, Raza HH, Khan IJ. First principles investigation of transition metal hydrides LiXH3 (X= Ti, Mn, and Cu) for hydrogen storage. J Comput Electr 2023;22:921–9.
[25] Gupta SL, Kumar S, Thakur SS, Kumar A, Panwar S. Effects of metals (X= Pd, Ag, Cd) on structural, electronic, mechanical, thermoelectric and hydrogen storage properties of LiXH3 perovskites. Computational and Theoretical Chemistry 2024;1241:114927.
[26] Yang S, Du M-H, Dong H-H, Li B-Y, Sun H-J, Qin W, et al. Ternary superconducting titanium hydrides stabilized via lithium. Phys B Condens Matter 2025:416971.
[27] Guo L, Chang L, Chen G, Zhang J. Structures and superconductivity of li–ti–h system under high pressure. J Alloys Compd 2025;1022:180140.
[28] Masood MK, Khan W, Bibi S, Kanwal A, Bibi S, Noor G, et al. Physical properties of the XScH3 (X: ca, and Mg) perovskite hydrides and their hydrogen storage applications. J Phys Chem Solid 2024;192:112098.
[29] Raza HH, Murtaza G, Khalil RMA. Optoelectronic and thermal properties of LiXH3 (X= Ba, Sr and Cs) for hydrogen storage materials: a first principle study. Solid State Commun 2019;299:113659.
[30] Lemziouka A, Azdad A, Lemziouka H, Boutahar A, Tahiri A, Mrharrab L. First-principles calculations to investigate structural, elastic, phonon, electronic, and optical properties of BaXH3 (X=Tc, Ta, and Mo) perovskite-type hydrides for hydrogen storage applications. J Power Sources 2025;653:237710. https://doi.org/10.1016/j.jpowsour.2025.237710.
[31] Benaali H, Bahhar S, Tahiri A, Didi Y, Fatihi H, Abbassi A, et al. Investigation of KMnH3 and KFeH3 perovskite hydrides via ab-initio for hydrogen storage. Inorg Chem Commun 2024;169:113033. https://doi.org/10.1016/j.inoche.2024.113033.
[32] Bahhar S, Jabar A, Tahiri A, Moubah R, Idiri M, Bioud H. X2CoH5 (X = Ca, Sr) for hydrogen storage: first-principles computations. Int J Hydrogen Energy 2024;83:1320–30. https://doi.org/10.1016/j.ijhydene.2024.08.155.
[33] Ermiş S, İyigör A, Kürkçü C. Investigation of K2TiH6 and Ca2TiH6 under pressures from 0 to 20 GPa: structural, electronic, thermodynamic, mechanical, vibrational, and hydrogen storage properties. Int J Hydrogen Energy 2025;177:151653. https://doi.org/10.1016/j.ijhydene.2025.151653.
[34] Antunes LM, Butler KT, Grau-Crespo R. Crystal structure generation with autoregressive large language modeling. Nat Commun 2024;15:10570. https://doi.org/10.1038/s41467-024-54639-7.
[35] Clark SJ, Segall MD, Pickard CJ, Hasnip PJ, Probert MIJ, Refson K, et al. First principles methods using CASTEP. Z Kristallogr Cryst Mater 2005;220:567–70. https://doi.org/10.1524/zkri.220.5.567.65075.
[36] Fischer TH, Almlof J. General methods for geometry and wave function optimization. J Phys Chem 1992;96:9768–74.
[37] Perdew JP, Burke K, Ernzerhof M. Generalized gradient approximation made simple. Phys Rev Lett 1996;77:3865.
[38] Vanderbilt D. Soft self-consistent pseudopotentials in a generalized eigenvalue formalism. Phys Rev B 1990;41:7892–5. https://doi.org/10.1103/PhysRevB.41.7892.
[39] Monkhorst HJ, Pack JD. Special points for Brillouin-zone integrations. Phys Rev B 1976;13:5188–92. https://doi.org/10.1103/PhysRevB.13.5188.
[40] Murtaza G, Yousaf N, Yaseen M, Laref A, Azam S. Systematic studies of the structural and optoelectronic characteristics of CaZn2X2 (X = N, P, As, Sb, Bi). Mater Res Express 2018;5:016304. https://doi.org/10.1088/2053-1591/aaa1c4.
[41] Ahmed R, Mahamudujjaman M, Afzal MA, Islam MS, Islam RS, Naqib SH. DFT based comparative analysis of the physical properties of some binary transition metal carbides XC (X = Nb, Ta, Ti). J Mater Res Technol 2023;24:4808–32. https://doi.org/10.1016/j.jmrt.2023.04.147.
[42] Morris AJ, Nicholls RJ, Pickard CJ, Yates JR. OptaDOS: a tool for obtaining density of states, core-level and optical spectra from electronic structure codes. Comput Phys Commun 2014;185:1477–85.
[43] Momma K, Izumi F. VESTA: a three-dimensional visualization system for electronic and structural analysis. J Appl Cryst 2008;41:653–8. https://doi.org/10.1107/S0021889808012016.
[44] Siddique A, Khalil A, Almutairi BS, Tahir MB, Ahsan T, Hannan A, et al. Structural, electronic, mechanical and dynamical stability properties of LiAH3 (A= Sc, Ti & V) perovskite-type hydrides: a first principle study. Chem Phys 2023;568:111851.
[45] Al S, Yamçıçır Ç. Computational exploration of hexahydride materials (K2SiH6 and Rb2SiH6); structural, mechanical, thermodynamic, optic, electronic and dynamic properties. J Energy Storage 2024;91:112033. https://doi.org/10.1016/j.est.2024.112033.
[46] Yamçıçır Ç, Kürkçü C. Structural, elastic, optic, electronic, phonon, thermodynamic, and hydrogen storage properties of bialkali alanates M2LiAlH6 (M = Na, K). Int J Hydrogen Energy 2025;135:440–56. https://doi.org/10.1016/j.ijhydene.2025.04.445.
[47] Masood MK, Khan W, Bibi S, Munir O, Timilsena S, Kanwal J, et al. The first principles investigation of free-lead perovskite-type hydrides CsXH3 (X= Sc, Y) for hydrogen storage application. Comput Theor Chem 2025;1246:115144.
[48] Khan W. The first principles insights of aluminum-based hydrides for hydrogen storage application. Int J Hydrogen Energy 2024;63:596–608.
[49] Yamçıçır Ç, Kürkçü C. Ab initio study of the structural, mechanical, optoelectronic and thermo-physical properties of XGaH5 (X=Ba, Ca, and Mg) compounds for hydrogen storage applications. Int J Hydrogen Energy 2024;81:391–404. https://doi.org/10.1016/j.ijhydene.2024.07.276.
[50] Mouhat N. Sufficient elastic stability conditions in various Hfystal systems. Phys Rev B n.d.
[51] Kleinman L. Deformation potentials in silicon. I. Uniaxial strain. Phys Rev 1962;128:2614–21. https://doi.org/10.1103/PhysRev.128.2614.
[52] Voigt W. Lehrbuch der kristallphysik (mit ausschluss der kristalloptik). Leipzig; Berlin. Ann Arbor, Mich: BG Teubner [JW Edwards; 1946.

[53] Reuss A. ZAMM-journal of applied mathematics and mechanics. Zeitschrift Fur Angewandte Mathematik Und Mechanik 1929;9:49.
[54] Hill R. First-principles elastic constants for the hcp transition metals Fe, Co, and re at high pressure. Proc Phys Soc 1952;65:350.
[55] Pugh SF. XCII. Relations between the elastic moduli and the plastic properties of polycrystalline pure metals. London, Edinburgh Dublin Phil Mag J Sci 1954;45:823–43.
[56] Wortman JJ, Evans RA. Young's modulus, shear modulus, and Poisson's ratio in silicon and germanium. J Appl Phys 1965;36:153–6.
[57] Mahamudujjaman Md, Afzal MdA, Islam RS, Naqib SH. First-principles insights into mechanical, optoelectronic, and thermo-physical properties of transition metal dichalcogenides ZrX2 (X = S, Se, and Te). AIP Adv 2022;12:025011. https://doi.org/10.1063/5.0073631.
[58] Tasnim A, Mahamudujjaman Md, Asif Afzal Md, Islam RS, Naqib SH. Pressure-dependent semiconductor–metal transition and elastic, electronic, optical, and thermophysical properties of orthorhombic SnS binary chalcogenide. Results Phys 2023;45:106236. https://doi.org/10.1016/j.rinp.2023.106236.
[59] Yamçıçır Ç. The analysis of structural, elastic, and electronic properties of Na3N compound under high hydrostatic pressure with the first principles method. Indian J Phys 2023;97:491–501. https://doi.org/10.1007/s12648-022-02545-3.
[60] Vitos L, Korzhavyi PA, Johansson B. Stainless steel optimization from quantum mechanical calculations. Nat Mater 2003;2:25–8.
[61] Phasha MJ, Ngoepe PE, Chauke HR, Pettifor DG, Nguyen-Mann D. Link between structural and mechanical stability of fcc-and bcc-based ordered Mg–Li alloys. Intermetallics 2010;18:2083–9.
[62] Sun Z, Music D, Ahuja R, Schneider JM. Theoretical investigation of the bonding and elastic properties of nanolayered ternary nitrides. Phys Rev B 2005;71:193402. https://doi.org/10.1103/PhysRevB.71.193402.
[63] Jhi S-H, Ihm J, Louie SG, Cohen ML. Electronic mechanism of hardness enhancement in transition-metal carbonitrides. Nature 1999;399:132–4. https://doi.org/10.1038/20148.
[64] Teter DM. Computational alchemy: the search for new superhard materials. MRS Bull 1998;23:22–7.
[65] Tian Y, Xu B, Zhao Z. Microscopic theory of hardness and design of novel superhard crystals. Int J Refract Metals Hard Mater 2012;33:93–106.
[66] Miao N, Sa B, Zhou J, Sun Z. Theoretical investigation on the transition-metal borides with Ta3B4-type structure: a class of hard and refractory materials. Comput Mater Sci 2011;50:1559–66.
[67] Mazhnik E, Oganov AR. A model of hardness and fracture toughness of solids. J Appl Phys 2019;126:125109.
[68] Chen X-Q, Niu H, Li D, Li Y. Modeling hardness of polycrystalline materials and bulk metallic glasses. Intermetallics 2011;19:1275–81.
[69] Naher MI, Naqib SH. First-principles insights into the mechanical, optoelectronic, thermophysical, and lattice dynamical properties of binary topological semimetal BaGa2. Results Phys 2022;37:105507.
[70] Yang P, Fu H, Guo X, Rachid B, Lin J. Mechanism of NbC as heterogeneous nucleus of M3C in CADI: first principle calculation and experiment research. J Mater Res Technol 2020;9:3109–20.
[71] Ahmed R, Mahamudujjaman M, Afzal MA, Islam MS, Islam R, Naqib S. Comparative analysis of physical properties of some binary transition metal carbides XC (X= Nb, Ta, Ti): insights from a comprehensive ab-initio study. arXiv Preprint arXiv:220911551 2022.
[72] Naher M, Naqib S. An ab-initio study on structural, elastic, electronic, bonding, thermal, and optical properties of topological Weyl semimetal Ta X (X= P, as). Sci Rep 2021;11:5592.
[73] Yamçıçır Ç, Kürkçü C. Investigation of structural, electronic, elastic, vibrational, thermodynamic, and optical properties of Mg2NiH4 and Mg2RuH4 compounds used in hydrogen storage. J Energy Storage 2024;84:110883. https://doi.org/10.1016/j.est.2024.110883.
[74] Yamçıçır S. First-principles investigation of structural, elastic, anisotropic, dynamic, electronic, thermo-physical, and optical properties of two-dimensional trigonal M2N (M = V, Nb, Ta) compounds for advanced technological applications. Phys B Condens Matter 2025;704:417070. https://doi.org/10.1016/j.physb.2025.417070.
[75] Kube CM. Elastic anisotropy of crystals. AIP Adv 2016;6.
[76] Vahldiek F. Anisotropy in single-crystal refractory compounds. Springer; 2013.
[77] Naher MI, Afzal MA, Naqib SH. A comprehensive DFT based insights into the physical properties of tetragonal superconducting Mo5PB2. Results Phys 2021;28:104612. https://doi.org/10.1016/j.rinp.2021.104612.
[78] Ravindran P, Fast L, Korzhavyi PA, Johansson B, Wills J, Eriksson O. Density functional theory for calculation of elastic properties of orthorhombic crystals: application to TiSi2. J Appl Phys 1998;84:4891–904. https://doi.org/10.1063/1.368733.
[79] Ran Z, Zou C, Wei Z, Wang H. VELAS: an open-source toolbox for visualization and analysis of elastic anisotropy. Comput Phys Commun 2023;283:108540. https://doi.org/10.1016/j.cpc.2022.108540.
[80] Rkhis M, Laasri S, Touhtouh S, Belhora F, Hlil E, Zaidat K, et al. Recent advances in magnesium hydride for solid-state hydrogen storage by mechanical treatment: a DFT study. Int J Hydrogen Energy 2023;48:35650–60.
[81] Siddique A, Khalil A, Almutairi BS, Tahir MB, Sagir M, Ullah Z, et al. Structures and hydrogen storage properties of AeVH3 (Ae= Be, Mg, Ca, Sr) perovskite hydrides by DFT calculations. Int J Hydrogen Energy 2023;48:24401–11.
[82] Tarasov BP, Fursikov PV, Volodin AA, Bocharnikov MS, Shimkus YY, Kashin AM, et al. Metal hydride hydrogen storage and compression systems for energy storage technologies. Int J Hydrogen Energy 2021;46:13647–57. https://doi.org/10.1016/j.ijhydene.2020.07.085.
[83] Khan W. Computational screening of BeXH3 (X: al, Ga, and in) for optoelectronics and hydrogen storage applications. Mater Sci Semicond Process 2024;174:108221. https://doi.org/10.1016/j.mssp.2024.108221.
[84] Anderson OL. A simplified method for calculating the Debye temperature from elastic constants. J Phys Chem Solid 1963;24:909–17.
[85] Schreiber E, Anderson OL, Soga N, Bell JF. Elastic constants and their measurement. 1975.
[86] Naher MI, Mahamudujjaman M, Tasnim A, Islam RS, Naqib SH. AbstAb-initio insights into the elastic, bonding, phonon, optoelectronic and thermophysical properties of SnTaS2. Solid State Sci 2022;131:106947.
[87] Brown LD, Fine ME, Marcus HL. Elastic constants versus melting temperature in metals. Scripta Metall 1984;18:951–6.
[88] Clarke DR. Materials selection guidelines for low thermal conductivity thermal barrier coatings. Surf Coat Technol 2003;163:67–74.
[89] Slack GA. The thermal conductivity of nonmetallic crystals. Solid State Phys 1979;34:1–71.
[90] Scarpati G, Frasci E, Di Ilio G, Jannelli E. A comprehensive review on metal hydrides-based hydrogen storage systems for mobile applications. J Energy Storage 2024;102:113934. https://doi.org/10.1016/j.est.2024.113934.
[91] El Akkel M, Ez-Zahraouy H. Novel double hydride perovskites Li2TiF6-xHx as efficient materials for solid-state hydrogen storage: DFT insights. Int J Hydrogen Energy 2025;101:1406–20. https://doi.org/10.1016/j.ijhydene.2025.01.023.
[92] Kalibek MR, Ospanova AD, Suleimenova B, Soltan R, Orazbek T, Makhmet AM, et al. Solid-state hydrogen storage materials. Discover Nano 2024;19:195. https://doi.org/10.1186/s11671-024-04137-y.
[93] Mulky L, Srivastava S, Lakshmi T, Sandadi ER, Gour S, Thomas NA, et al. An overview of hydrogen storage technologies – key challenges and opportunities. Mater Chem Phys 2024;325:129710. https://doi.org/10.1016/j.matchemphys.2024.129710.
[94] Global hydrogen review 2023. 2023.
[95] Orimo S, Nakamori Y, Eliseo JR, Züttel A, Jensen CM. Complex hydrides for hydrogen storage. Chem Rev 2007;107:4111–32. https://doi.org/10.1021/cr0501846.
[96] Züttel A. Materials for hydrogen storage. Mater Today 2003;6:24–33. https://doi.org/10.1016/S1369-7021(03)00922-2.
[97] El Mekkaouy A, Akarchaou EH, Tahiri A, Chtita S, Touti R. First principles computational study of X2CaTiH6 (X =Li, and Na) for hydrogen storage applications. Int J Hydrogen Energy 2025;164:150723. https://doi.org/10.1016/j.ijhydene.2025.150723.
[98] Didi Y, El Fatouaki Z, Touti R, Ahfir R, Tahiri A, Naji M, et al. First principles computational study of MgX3H8 (X=V and Fe) for hydrogen storage applications. Int J Hydrogen Energy 2025;133:140–51. https://doi.org/10.1016/j.ijhydene.2025.04.265.
[99] El Fatouaki Z, Tahiri A, Jabar A, Idiri M. First-principles study on the physical properties of double perovskites LiX3H8 (X = Ni and Mn) for hydrogen storage. J Phys Chem Solid 2025;206:112867. https://doi.org/10.1016/j.jpcs.2025.112867.
[100] El Fatouaki Z, Hrida EM, Tahiri A, Jabar A, Idiri M. Comprehensive first-principles and AIMD study of alkali metal LiX3H8 (X = Fe, Cr) hydrides for hydrogen storage applications. Int J Hydrogen Energy 2025;163:150791. https://doi.org/10.1016/j.ijhydene.2025.150791.
[101] Aafi K, El Fatouaki Z, Jabar A, Tahiri A, Idiri M. New alkali metal compounds XCo3H8 (X = Li, Na and K) for hydrogen storage technology. J Phys Chem Solid 2025;208:113064. https://doi.org/10.1016/j.jpcs.2025.113064.
[102] Akarchaou EH, Touti R, El Mekkaouy A, Didi Y, Tahiri A, Chtita S. Computational analysis of X2MgTiH6 (X =Li, Na, and K) double perovskite hydride materials for hydrogen storage applications. Int J Hydrogen Energy 2025;161:150644. https://doi.org/10.1016/j.ijhydene.2025.150644.
[103] Zeng Q, Su K, Zhang L, Xu Y, Cheng L, Yan X. Evaluation of the thermodynamic data of CH3SiCl3 based on Quantum chemistry calculations. J Phys Chem Ref Data 2006;35:1385–90. https://doi.org/10.1063/1.2201867.
[104] Lyu J, Elman R, Svyatkin L, Kudiiarov V. Theoretical and experimental research of hydrogen storage properties of Mg and Mg-Al hydrides. J Alloys Compd 2023;938:168618.
[105] Didi Y, Bahhar S, Tahiri A, Naji M, Rjeb A. A computational study of metal hydrides based on rubidium for developing solid-state hydrogen storage. ChemistrySelect 2024;9:e202401444. https://doi.org/10.1002/slct.202401444.